INTERNATIONAL JOURNAL FOR NUMERICAL METHODS IN ENGINEERING
Int. J. Numer. Meth. Engng 2011; **88**:279–306
Published online 22 March 2011 in Wiley Online Library (wileyonlinelibrary.com). DOI: 10.1002/nme.3176

A statistical method for verifying mesh convergence in Monte Carlo simulations with application to fragmentation

J. E. Bishop[1,*,†] and O. E. Strack[2]

[1]*Computational Structural Mechanics, Sandia National Laboratories, Albuquerque, NM 87185, U.S.A.*
[2]*Computational Shock and Multiphysics, Sandia National Laboratories, Albuquerque, NM 87185, U.S.A.*

SUMMARY

A novel method is presented for assessing the convergence of a sequence of statistical distributions generated by direct Monte Carlo sampling. The primary application is to assess the mesh or grid convergence, and possibly divergence, of stochastic outputs from non-linear continuum systems. Example systems include those from fluid or solid mechanics, particularly those with instabilities and sensitive dependence on initial conditions or system parameters. The convergence assessment is based on demonstrating empirically that a sequence of cumulative distribution functions converges in the L_∞ norm. The effect of finite sample sizes is quantified using confidence levels from the Kolmogorov–Smirnov statistic. The statistical method is independent of the underlying distributions.

The statistical method is demonstrated using two examples: (1) the logistic map in the chaotic regime, and (2) a fragmenting ductile ring modeled with an explicit-dynamics finite element code. In the fragmenting ring example the convergence of the distribution describing neck spacing is investigated. The initial yield strength is treated as a random field. Two different random fields are considered, one with spatial correlation and the other without. Both cases converged, albeit to different distributions. The case with spatial correlation exhibited a significantly higher convergence rate compared with the one without spatial correlation.

Received 3 August 2010; Revised 13 January 2011; Accepted 23 January 2011

KEY WORDS: verification; convergence in distribution; Kolmogorov–Smirnov statistic; optimization; fragmentation; Monte Carlo

1. INTRODUCTION

Engineers and scientists are increasingly challenged to simulate ever more complex physical phenomena, from the response of structures under extreme loading events, such as car crashes, to the long term behavior of the Earth's climate. Owing to the high-consequence decisions made using such simulations, it is important that the mathematical models and their numerical approximations be verified and validated [1, 2]. Verification is concerned with assessing the accuracy of a numerical approximation to the solution of a mathematical model. Validation is concerned with ensuring that the mathematical model is an adequate description of reality by comparison with experimental data [3, 4]. Many models of macroscopic phenomena are based on continuum theories represented as partial differential equations or integral equations. For these models one necessary condition for verification is that numerical approximations of the solution converge with discretization refinement. Without convergence, numerical results are unreliable, rendering subsequent validation, uncertainty

*Correspondence to: J. E. Bishop, Sandia National Laboratories, P.O. Box 5800, Mail Stop 0372, Albuquerque, NM 87185-0372, U.S.A.
†E-mail: jebisho@sandia.gov

quantification efforts, and general use in engineering design and scientific prediction unreliable as well. An interesting example of nonconvergence with mesh refinement has been demonstrated by Meulbroek *et al.* [5] in their modeling of a fragmenting ductile ring using an Eulerian hydrocode.

For stochastic systems the task of verification is particularly challenging as one now has to deal with issues related to the probability domains. The stochastic dimension of a system refers to the number of random variables in the state description. For many uncertainty quantification methods the computational cost increases dramatically as the stochastic dimension increases. An overview of several methods for uncertainty quantification in engineering applications is given by Schuëller and Pradlwarter [6] including perturbation procedures, expansion methods such as Karhunen–Loève and polynomial chaos expansions, as well as direct and advanced Monte Carlo sampling. Monte Carlo sampling refers to methods in which a set of simulations is run with input values for each simulation obtained by sampling the distributions of the input parameters. Based on the simulation results, approximate distribution functions can be formed for output quantities of interest. Direct Monte Carlo sampling indicates that sampling of the input parameters is unbiased, while advanced Monte Carlo sampling refers to techniques such as importance sampling in which sampling is biased to maximize information in regions of interest. For systems with low stochastic dimension, the expansion methods are particularly effective [7, 8], although their series convergence may be slow in highly non-linear problems with instabilities and bifurcations [9–12]. Although the current numerical limit for which expansion methods are computationally feasible is steadily increasing [13], for systems with high stochastic dimension one must still resort to Monte Carlo sampling [6]. Examples of systems with high stochastic dimension include those from porous flow, fluid dynamics, and solid dynamics in which the spatially dependent parameters are treated as random fields with relatively small correlation lengths. The Monte Carlo method converges with increasing sample size at a rate that is independent of the stochastic dimension, but typically requires large sample sizes to achieve the required accuracy.

There are instances in engineering practice when a numerical method is used or enhanced to simulate physical behavior that is outside the original well-posed mathematical formulation. For example, in structural mechanics it is well known that ductile fracture is preceded by material softening, a constitutive effect, which causes the governing system of equations to become ill-posed; the effect is a mesh dependency in the associated discretized problem [14, 15]. In addition, 'element erosion' or 'element death' is often used in Lagrangian finite element simulations to model arbitrary fracture [16]. Many physical systems that involve material softening and fracture are stochastic in nature, such as pervasive fracture processes [17] and fragmentation [18]. Monte Carlo simulations of these stochastic systems will have finite-sampling errors in the empirical cumulative distribution function (CDF) that are on the order of $1/\sqrt{N}$, where N is the sample size. An accurate assessment of mesh convergence must quantify these finite sampling effects, for example, with confidence intervals. If sample sizes are too small (confidence intervals too large), mesh convergence rates may be inaccurate, and may even fail to detect mesh divergence. An empirical demonstration of convergence is, however, only one step in the verification process. A broader task is verifying that the converged distribution is a unique solution of the original mathematical model.

In this paper, a statistical method is presented for assessing the convergence properties of a sequence of CDFs generated by direct Monte Carlo sampling. The Kolmogorov–Smirnov (KS) statistic is used to quantify the error in the sampled CDFs due to finite sample sizes. An important property of the KS statistic is that it is independent of the particular form of the CDF, and assumes only that the CDF is continuous. Herein, the KS statistic is used to assess the confidence level on the L_∞ distance between two sampled CDFs. With at least three mesh resolutions and sufficiently large sample sizes at each mesh resolution, a mesh convergence rate can be estimated. Conversely, given a postulated mesh convergence rate, the required sample size necessary to resolve the mesh discretization error can be estimated. One of the main challenges in verifying convergence is the large sample sizes required. To partially address this issue an optimization problem is formulated that minimizes total ensemble simulation cost over the space of sample sizes, given constraints on sampling accuracy. The optimization problem is solved using the method of Lagrange multipliers. The statistical method is demonstrated using two examples: (1) a logistic map that has been

DOI: 10.1002/nme

spatially discretized with piecewise-linear segments and (2) a fragmenting ductile ring modeled with an explicit-dynamics finite element code. For the second example, the convergence behavior of the critical neck statistics is investigated for two different random field representations of the initial yield strength, one with spatial correlation and the other without.

Recently, the use of the L_1 distance has been proposed by Roy and Oberkampf [19, 20] for use in model validation by comparing sampled CDFs from both experiments and model simulations. However, a statistic characterizing the effect of finite sample sizes was not presented. Some advantages of using L_1 distance as opposed to the L_∞ distance are discussed in Section 8. Our future research will focus on comparing and contrasting these and other distance functions.

This paper is organized as follows. Section 2 reviews the definitions of the CDF, the probability distribution function, and convergence in distribution. Section 3 reviews the KS statistic and discusses the deleterious effects of quantization and correlated sampling. Section 4 presents the statistical method for assessing convergence in distribution. The method is applied to two examples: (1) the chaotic logistic map in Section 5 and (2) a fragmenting ductile ring modeled with an explicit-dynamics finite element code in Section 6. The optimization problem of minimizing total ensemble simulation cost given constraints on sampling accuracy is formulated and solved in Section 7. Finally, conclusions and discussion of the future work are given in Section 8.

2. CONVERGENCE IN DISTRIBUTION

In this section, the definitions of the CDF, the probability distribution function, and convergence in distribution are briefly reviewed. A more detailed discussion of these concepts, and probability theory in general, is given in References [21, 22].

A real-valued random variable is a function Y that maps a sample space Ω into the real numbers $\mathbb{R}$. For the fragmenting ring example given in Section 6 the sample space is the set of all possible fragments resulting from all possible simulations. In this case several random variables are possible including fragment volume, fragment momentum, and fragment temperature. These are continuous random variables, as opposed to discrete random variables such as number-of-fragments. A probability measure $\mathscr{P}$ is a mapping of subsets of the sample space Ω into the unit interval [0,1] with $\mathscr{P}(\emptyset)=0$, $\mathscr{P}(\Omega)=1$, such that $\mathscr{P}$ is countably additive [22]. The distribution of probability of the random variable Y is characterized by the CDF $F(y)$ defined as

$$F(y):=\mathscr{P}\{\omega\in\Omega;\, Y(\omega)\leqslant y\},\quad y\in\mathbb{R} \text{ or simply } F(y):=\mathscr{P}(Y\leqslant y). \tag{1}$$

The CDF gives the probability that the random variable Y has a value less than or equal to y. The CDF of a random variable has the following properties [21, Ch. 3.2]:

(1) $0\leqslant F(y)\leqslant 1$ for all y, and $\lim_{y\to-\infty}F(y)=0$ and $\lim_{y\to\infty}F(y)=1$,
(2) $F(y)$ is non-decreasing: $F(y_1)\leqslant F(y_2)$ whenever $y_1<y_2$,
(3) $F(y)$ is right-continuous: $\lim_{y\to a^+}F(y)=F(a)$,
(4) $\mathscr{P}(a<Y\leqslant b)=F(b)-F(a)\geqslant 0$ for $a\leqslant b$.

If $F(y)$ is differentiable, then the probability density function (PDF) is defined as

$$f(y):=\frac{\mathrm{d}F(y)}{\mathrm{d}y}. \tag{2}$$

As an example consider a random variable with a CDF given by the two-parameter Weibull distribution [23]

$$F(y)=\begin{cases}1-\mathrm{e}^{-(y/\gamma)^\eta}, & y\geqslant 0,\\ 0, & y<0,\end{cases} \tag{3}$$

DOI: 10.1002/nme

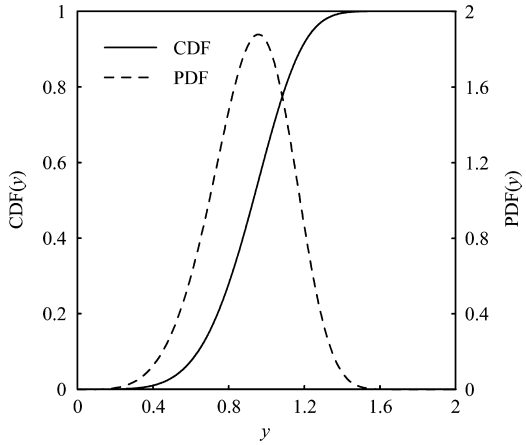

Figure 1. The CDF and PDF of the two-parameter Weibull distribution defined in Equations (3) and (4), respectively, with $\eta=5$ and $\gamma=1$.

where $\eta>0$ is the shape parameter (or modulus), and $\gamma>0$ is the scale parameter. The Weibull PDF is given by

$$f(y)=\begin{cases}\dfrac{\eta}{\gamma}\left(\dfrac{y}{\gamma}\right)^{\eta-1}\mathrm{e}^{-(y/\gamma)^{\eta}}, & y\geqslant 0,\\ 0, & y<0.\end{cases} \tag{4}$$

Figure 1 shows the Weibull CDF and PDF for $\eta=5$ and $\gamma=1$. The two-parameter Weibull distribution will be used in the example given in Section 6.

For a collection of random variables Y_h with real index $h>0$, it is possible to explore the limit of Y_h as $h\to 0$. If this limit exists and is equal to the random variable Y, then Y_h is said to converge to Y as $h\to 0$. In the case of random variables there are a number of different modes in which this convergence may be understood. These are *almost sure convergence*, *convergence in probability*, and *convergence in distribution* [24, Ch. 6]. Each mode of convergence may be stronger or weaker than another according to whether convergence in one mode implies the other. Convergence in distribution does not, in general, imply the other two modes of convergence. However, both almost sure convergence and convergence in probability imply convergence in distribution. The focus of this paper is convergence in distribution. Let F_h and F be the CDFs of the random variables Y_h and Y, respectively. The random variable Y_h is said to converge in distribution to Y if

$$\lim_{h\to 0} F_h(y)=F(y) \tag{5}$$

for all $y\in\mathbb{R}$ such that F is continuous [24, Ch. 6].

Now consider a physical system and an associated mathematical model. If the model is well-posed, then a numerical approximation to the model should converge to a unique solution with discretization refinement. Actually verifying this convergence for complex non-linear multiphysics models can be challenging. Consider a sequence of model discretizations $\mathscr{H}_1, \mathscr{H}_2, \ldots$ with corresponding mesh sizes $h_1, h_2, \ldots$ where the mesh sizes satisfy $h_j<h_i$ for all $j>i$. In engineering practice, convergence is empirically verified by examining a quantity of interest y and its approximation y_h as $h\to 0$. If the physical system is stochastic in nature then the quantity of interest will be a random variable Y with an associated CDF $F(y)$. The sequence of model discretizations will produce a sequence of CDFs $F_1(y), F_2(y), \ldots$. However, each CDF $F_i(y)$ itself can only be approximated using, for example, uncertainty quantification methods [6]. The focus of this paper is the method of direct Monte Carlo sampling. The following two sections develop a statistical method for assessing convergence in distribution of a sequence of CDFs $F_1(y), F_2(y), \ldots$ where each CDF is approximated with direct Monte Carlo sampling.

DOI: 10.1002/nme

3. KOLMOGOROV–SMIRNOV STATISTIC

A key aspect of verifying convergence in distribution using direct Monte Carlo sampling is quantifying the effect of finite sample sizes. Here, this sampling error is quantified using the KS statistic [25]. The KS statistic is widely used in non-parametric statistical testing [26] and is briefly reviewed in this section. An important property of the KS statistic is that it is distribution free (independent of the actual form of $F(y)$). The main restriction on the use of the KS statistic is the assumption of a continuous CDF, which precludes the use of discrete random variables. (In many cases a discrete quantity of interest can be exchanged for a continuous one. For example, in a fragmentation simulation the continuous quantity fragment mass could be used in place of the discrete quantity number-of-fragments.)

The KS statistic is based on the sample CDF or empirical CDF (eCDF) defined as follows [27]. Let $\{y_i\}$ be a set of N independent and identically distributed random samples. The eCDF $S_N(y)$ is defined as the proportion of samples not exceeding y

$$S_N(y) := \begin{cases} 0, & y < y_1, \\ \dfrac{r}{N}, & y_r \leqslant y < y_{r+1}, \quad r = 1, \ldots, N-1, \\ 1, & y_N \leqslant y, \end{cases} \tag{6}$$

where $(y_1, y_2, \ldots, y_N)$ are the samples arranged in increasing order. If $F(y)$ is the CDF of the random variable from which the samples are drawn, then the Strong Law of Large Numbers gives that $S_N(y)$ converges almost surely to $F(y)$ as $N \to \infty$ [24, Ch. 7]. In other words, as the sample size gets larger the eCDF is expected (in a probabilistic sense) to become an increasingly more accurate approximation to the CDF. This probability is quantified using the KS statistic.

The KS statistic D_N is defined as the L_∞ distance between $S_N(y)$ and $F(y)$

$$D_N := \|S_N(y) - F(y)\|_\infty := \sup_{y \in \mathbb{R}} |S_N(y) - F(y)|. \tag{7}$$

An asymptotic distribution ($N \to \infty$) for D_N was first derived by Kolmogorov in 1933 [25]

$$\lim_{N \to \infty} \mathscr{P}(D_N \leqslant z/\sqrt{N}) = 1 - 2 \sum_{j=1}^{\infty} (-1)^{j-1} \exp(-2j^2 z^2) := p(z). \tag{8}$$

This result gives the probability that the KS statistic D_N will be less than a certain value z for a given sample size N. The function $p(z)$ is plotted in Figure 2. In particular, $p(1.3581) = 0.95$ and $p(1.6276) = 0.99$. Equation (8) then gives

$$\mathscr{P}\left(D_N \leqslant \frac{1.3581}{\sqrt{N}}\right) = 0.95 \quad \text{and} \quad \mathscr{P}\left(D_N \leqslant \frac{1.6276}{\sqrt{N}}\right) = 0.99 \quad \text{for } N \to \infty. \tag{9}$$

The quantity to the right of each inequality within the parentheses represents the critical value of D_N for the given probabilities $p(z) = 0.95$ and $p(z) = 0.99$. Birnbaum [28] used recurrence relations originally derived by Kolmogorov [25] to obtain the critical values of D_N for any N. Birnbaum observed that the asymptotic distribution given by Equation (8) is conservative and accurate to within 2% for $N > 50$ [28]. In practice, the assessment of convergence in distribution through Monte Carlo sampling will require sample sizes much larger than 50, so that the asymptotic relations in Equation (9) are more than adequate. The following method development, however, is not dependent upon this approximation. The tabulated critical values of D_N for $N < 50$ could be used if required.

Because the measure of sample divergence (Equation (7)) is the maximum absolute deviation between $S_N(y)$ and $F(y)$, D_N may be used to set confidence limits for the entire eCDF [27]. Let

DOI: 10.1002/nme

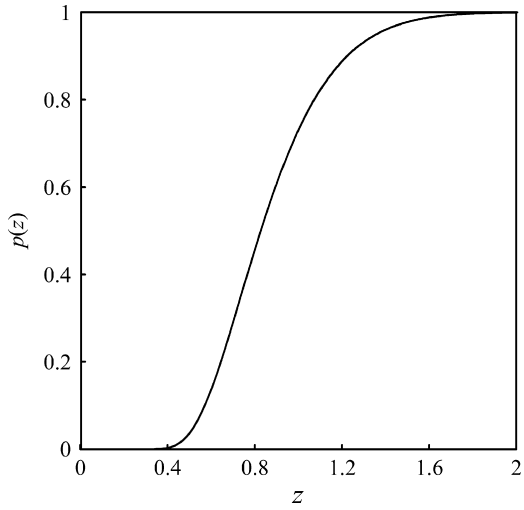

Figure 2. The Kolmogorov distribution defined in Equation (8).

d_α represent the critical value of D_N for probability $p(z)=1-\alpha$. Here, α is commonly called the significance level and $1-\alpha$ the confidence level. In particular, from Equation (9),

$$d_{0.05}=\frac{1.3581}{\sqrt{N}} \quad \text{and} \quad d_{0.01}=\frac{1.6276}{\sqrt{N}}. \tag{10}$$

It follows from Equation (8) that

$$\mathscr{P}\left(D_N=\sup_{y\in\mathbb{R}}|S_N(y)-F(y)|>d_\alpha\right)=\alpha. \tag{11}$$

This statement may be inverted into the confidence statement

$$\mathscr{P}[S_N(y)-d_\alpha\leqslant F(y)\leqslant S_N(y)+d_\alpha,\ \forall y\in\mathbb{R}]=1-\alpha. \tag{12}$$

Thus, there is a band of width $\pm d_\alpha$ around the eCDF $S_N(y)$, and there is probability (confidence) $1-\alpha$ that the CDF $F(y)$ lies completely within this band [27]. An equivalent interpretation is a band of width $\pm d_\alpha$ around the CDF $F(y)$, and there is probability $1-\alpha$ that the eCDF $S_N(y)$ lies completely within the band

$$\mathscr{P}[F(y)-d_\alpha\leqslant S_N(y)\leqslant F(y)+d_\alpha,\ \forall y\in\mathbb{R}]=1-\alpha. \tag{13}$$

The confidence limits can be used to estimate the sample size required to approximate the CDF with a given accuracy. Suppose one is interested in approximating the CDF with an accuracy of 10% with 95% confidence ($\mathscr{P}(D_N\leqslant 0.1)=0.95$). From the first relation of Equation (9), a sample size of $(1.3581/0.1)^2\approx 184$ is needed. To approximate the CDF with an accuracy of 1% with 95% confidence ($\mathscr{P}(D_N\leqslant 0.01)=0.95$) requires a sample size of $(1.3581/0.01)^2\approx 18\,444$.

In order to visualize these results consider the two-parameter Weibull probability distribution shown in Figure 1. Figure 3 shows sample eCDFs for two sample sizes: (a) $N=50$ and (b) $N=500$. The 95% confidence intervals are also shown, and the resulting KS statistic is identified. For the sample size $N=50$ the critical KS statistic is $d_{0.05}=1.36/\sqrt{50}=0.19$. For the given sample the KS statistic is $D=0.1$, which is less than the critical value. For the sample size $N=500$ the critical KS statistic is $d_{0.05}=1.36/\sqrt{500}=0.06$. For the given sample the KS statistic is $D=0.03$, which is again less than the critical value. For these particular samples, the eCDFs fall within the 95% confidence band.

DOI: 10.1002/nme

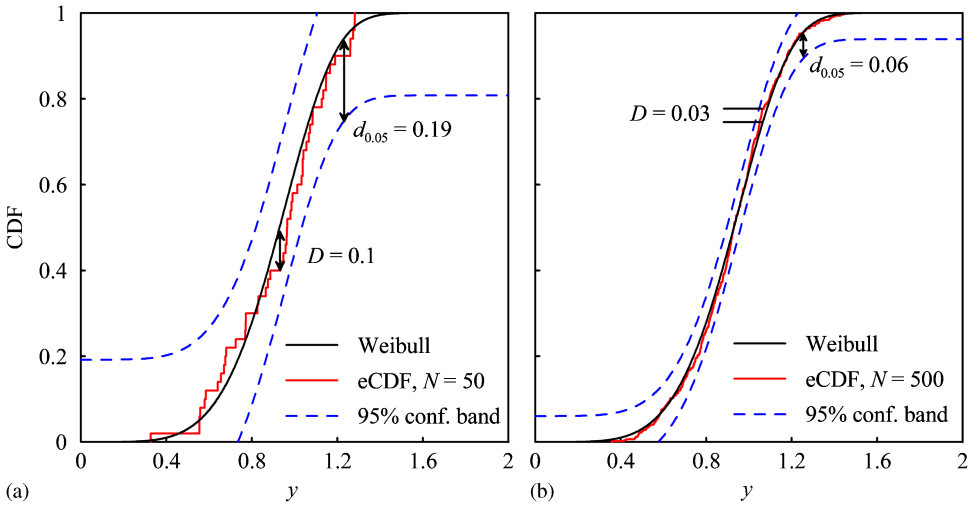

Figure 3. Example of the Kolmogorov–Smirnov statistic applied to the two-parameter Weibull distribution shown in Figure 1. Sample eCDFs are shown for two sample sizes: (a) $N = 50$ and (b) $N = 500$. The resulting KS statistic D is identified. The 95% confidence bands are also shown.

3.1. Cluster sampling

In the field of statistics, there are several types of sampling techniques. These include simple random sampling (the most commonly used sampling technique), stratified random sampling, cluster sampling, systematic sampling [29, Ch. 2], and importance sampling [30]. In simple random sampling, each element of the sample space is equally probable, that is, there is no bias in choosing the samples. The KS statistic is predicated on the use of simple random sampling. This requirement on the KS statistic precludes the use of Monte Carlo methods that use importance sampling [30]. In cluster sampling, the sample space is first partitioned into groups or clusters. A simple random sample is then taken from the collection of clusters, and each cluster is then subsampled. Fragmentation modeling is, in effect, cluster sampling. In fragmentation simulations several fragments are created in a single simulation (see Section 6). In this case, each simulation is a cluster. Cluster sampling could be deleterious if the sampling results are interpreted as being a simple random sample [31]. In particular, the confidence bounds developed in Section 3 could be inaccurate. For example, in fragmentation modeling an extreme case would occur if all fragments in a simulation were of nearly equal size, but the fragment size varied from simulation to simulation. In this case there would be no variation within a cluster, unlike the full population. A simple random sample could be obtained in this case by using only one (random) fragment per simulation.

Several statistics exist that can be used to test whether a cluster sample can be used as a simple random sample. One example is the intracluster correlation coefficient which provides a measure of homogeneity within the clusters, but is only defined for clusters of equal sizes [29, Ch. 5]. An alternative measure is the adjusted population correlation coefficient, R_a^2, defined as [29, Ch. 5]

$$R_a^2 := 1 - \frac{S_c^2}{S^2}. \tag{14}$$

Here, S_c^2 is the aggregate of within-cluster variances, and S^2 is the variance of the entire sample

$$S_c^2 := \frac{1}{\sum_{i=1}^{N}(M_i - 1)} \sum_{i=1}^{N} \sum_{j=1}^{M_i} (y_{ij} - \overline{y}_i)^2 \tag{15}$$

DOI: 10.1002/nme

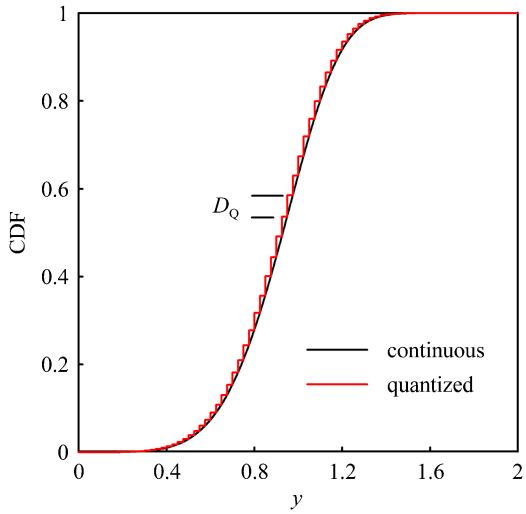

Figure 4. Effect of quantization on an otherwise continuous cumulative distribution function. The quantization level is $\Delta y = 0.025$, and the error in the KS statistic due to quantization is $D_Q = 0.04$.

and

$$S^2 := \frac{1}{\left(\sum_{i=1}^{N} M_i\right) - 1} \sum_{i=1}^{N} \sum_{j=1}^{M_i} (y_{ij} - \overline{y})^2, \tag{16}$$

where y_{ij} represents the jth sample from ith cluster, $\overline{y}$ is the entire sample mean, $\overline{y}_i$ is the mean of the ith cluster, N represents the number of clusters, and M_i represents the size of cluster i. R_a^2 is typically positive since quantities within a cluster tend to be more similar than quantities selected at random from the full population [29, Ch. 5]. The extreme case would be if all elements within a cluster were identical causing the numerator in Equation (14) to be zero and $R_a^2 = 1$. For the use of a cluster sample as a simple random sample, R_a^2 should be close to zero. This test will be applied to the example problem given in Section 6.

3.2. *Quantization effect*

In digital calculations there is an inherent discretization and quantization of continuous variables due to finite precision. This quantization will cause an otherwise continuous CDF to be piecewise constant as illustrated in Figure 4. Since the KS statistic applies only to continuous CDFs, an error D_Q is introduced. The quantization of continuous variables can arise from the mesh or grid discretization as well. For example, consider a Lagrangian finite element simulation of a fragmentation process. Since each fragment is the aggregate of finite elements, the fragment volume is quantized at the level of the finite element volume. These quantization effects prevent the KS statistic from approaching zero as $N \to \infty$. The example problem given in Section 6 will demonstrate this effect.

If the CDF is differentiable then D_Q is given by

$$D_Q = \max_{y \in \mathbb{R}} \left(\frac{\mathrm{d}F}{\mathrm{d}y} \right) \Delta y, \tag{17}$$

where Δy represents the quantization magnitude. In Figure 4, $D_Q = 0.04$ which could be resolved with a sample size of $N = 1153$ at the 95% confidence level (from Equation (9)). It would therefore be futile to increase the sample size beyond $N = 1153$. If Δy is due to the domain discretization, then D_Q will converge to zero as the discretization length decreases. However, depending upon this convergence rate and sample size, D_Q may or may not be greater than the sampling error. For the fragmentation example given in Section 6, the fragment quantization will decrease with

DOI: 10.1002/nme

order h since the problem is quasi one dimensional, whereas in a full 3D fragmentation problem the fragment quantization will decrease with order h^3.

4. ASSESSING CONVERGENCE IN DISTRIBUTION

Consider a sequence of continuous CDFs, $F_i(y)$, $i=1,2,\ldots$. To be consistent with the KS statistic defined in Equation (7), the L_∞ norm is used to measure the distance between two CDFs, $F_i(y)$ and $F_j(y)$

$$\|F_i(y)-F_j(y)\|_\infty := \sup_{y\in\mathbb{R}} |F_i(y)-F_j(y)|. \tag{18}$$

Since the limit of $F_i(y)$ as $i\to\infty$ is typically unknown, the assessment of convergence in distribution will be based on verifying that the sequence is Cauchy. A sequence of continuous functions $F_i(y)$, $i=1,2,\ldots$, is Cauchy in the L_∞ norm if for each $\varepsilon>0$ there exists an $n(\varepsilon)$ for which $\|F_i(y)-F_j(y)\|_\infty<\varepsilon$ whenever $i>n$ and $j>n$. Since the space of continuous functions with the L_∞ norm is complete, so that any Cauchy sequence of continuous functions is uniformly convergent to a continuous function [32], it follows that if a sequence of continuous CDFs is Cauchy in the L_∞ norm, then the limit CDF is also continuous. Furthermore, from Equation (5) the sequence converges in distribution. In practice, convergence will be empirically assessed or verified by examining the sequential pairwise L_∞ distance in the first few terms of a mesh refinement study. If the pairwise distance converges to zero with order h^β, then this is strong evidence that the full sequence is convergent [3].

Consider now two CDFs, $F_i(y)$ and $F_j(y)$, in the discretization sequence and their eCDFs, $S_{N_i}(y)$ and $S_{N_j}(y)$, obtained through Monte Carlo sampling with sample sizes N_i and N_j, respectively, as shown in Figure 5. Let the normed difference between the two CDFs, as defined by Equation (18), be denoted $d_{i,j}$. Similarly, let the normed difference between the two eCDFs be denoted by d_{N_i,N_j}. The normed difference between the CDF $F_i(y)$ and its eCDF $S_{N_i}(y)$ is the KS statistic D_{N_i} defined in Equation (7). This distance is bounded by the critical value d_{α_i} as described by Equation (13). Similarly, let D_{N_j} represent the normed difference between the CDF $F_j(y)$ and its eCDF $S_{N_j}(y)$. This distance is bounded by the critical value d_{α_j}. These distances are shown schematically in Figure 5. A confidence statement on the difference between the true distance $d_{i,j}$ and the sampled distance d_{N_i,N_j} is given by

$$\mathscr{P}[|d_{i,j}-d_{N_i,N_j}|\leqslant d_{\alpha_i}+d_{\alpha_j}=z_i/\sqrt{N_i}+z_j/\sqrt{N_j}]=(1-\alpha_i)(1-\alpha_j), \tag{19}$$

where z_i and z_j are a function of the chosen significance levels α_i and α_j, respectively, as demonstrated in Equation (9). Equation (19) can be derived as follows. By inspection of Figure 5 we see that

$$d_{i,j}+d_{\alpha_i}+d_{\alpha_j}\geqslant d_{N_i,N_j}\Rightarrow d_{N_i,N_j}-d_{i,j}\leqslant d_{\alpha_i}+d_{\alpha_j}. \tag{20}$$

Similarly

$$d_{N_i,N_j}+d_{\alpha_i}+d_{\alpha_j}\geqslant d_{i,j}\Rightarrow -(d_{N_i,N_j}-d_{i,j})\leqslant d_{\alpha_i}+d_{\alpha_j}. \tag{21}$$

Combining these two equations gives

$$|d_{i,j}-d_{N_i,N_j}|\leqslant d_{\alpha_i}+d_{\alpha_j}. \tag{22}$$

From Equation (13) the probability that the eCDF of distribution i is in the band $F_i(y)\pm d_{\alpha_i}$ is $1-\alpha_i$ and the probability that the eCDF of distribution j is in the band $F_j(y)\pm d_{\alpha_j}$ is $1-\alpha_j$. Assuming independence, the joint probability is thus $(1-\alpha_i)(1-\alpha_j)$. The sampled distance d_{N_i,N_j} can now be reported using a confidence bound, $d_{N_i,N_j}\pm(z_i/\sqrt{N_i}+z_j/\sqrt{N_j})$.

Equation (19) can also be used to estimate the required sample size in order to resolve a distance $d_{i,j}$ between two CDFs. However, since the true distance $d_{i,j}$ is not in general known *a priori*

DOI: 10.1002/nme

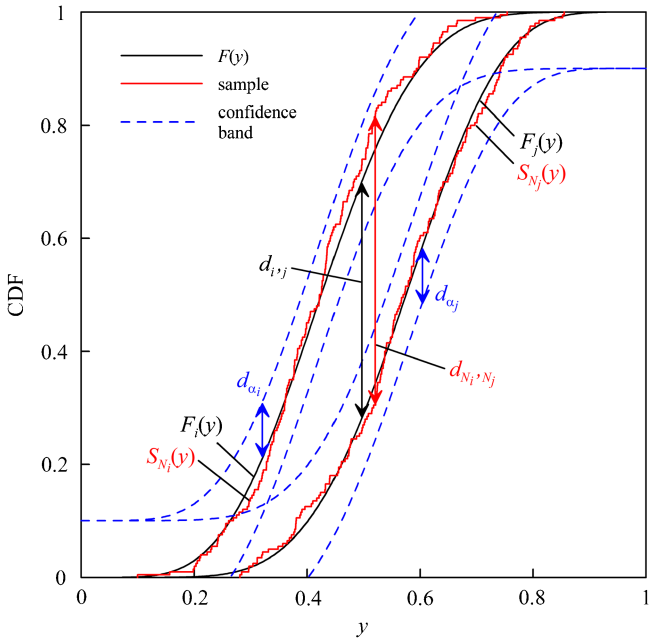

Figure 5. Nomenclature used in the proof of Equation (19). Two CDFs, $F_i(y)$ and $F_j(y)$, the eCDFs of their samples, $S_{N_i}(y)$ and $S_{N_j}(y)$, and their confidence bounds, are shown along with L_∞ distances.

but only the sampled distance d_{N_i,N_j}, the mutual sample sizes N_i and N_j have to increase until the sampled distance is resolved by the confidence band to an acceptable accuracy. To this end, a relative sampling accuracy δ is defined as

$$\delta := \frac{z_i/\sqrt{N_i} + z_j/\sqrt{N_j}}{d_{i,j}}. \tag{23}$$

The true distance $d_{i,j}$ is estimated via d_{N_i,N_j} as the ensemble sampling progresses resulting in an estimated relative sampling accuracy δ_{est}.[‡] Choosing a value of δ (e.g. 0.1), N_i and N_j may be increased uniformly until $\delta_{\text{est}} \leqslant \delta$. Similarly, for a sequence of n mesh levels, the following algorithm may be used:

for $i = 1 : n-1$
  Choose a relative sampling accuracy δ with $0 < \delta < 1$.
  Choose significance levels α_i and α_{i+1}.
  do
    Increase sample sizes N_i and N_{i+1} uniformly for mesh levels i and $i+1$.
    Calculate $d_{N_i,N_{i+1}}$ and δ_{est}.
  loop until $(\delta_{\text{est}} \leqslant \delta)$
next i

Note that this algorithm suggests increasing uniformly the sample sizes within a pair of mesh levels. In practice, the 'cost' of a simulation increases significantly with an increase in mesh refinement. Thus, it is advantageous to minimize the number of samples at the more refined mesh level. A method for estimating minimal sample sizes for a sequence of meshes for several cost functions is given in Section 7. For a cost function that is independent of mesh size, a simple

[‡]For the example problems in this paper, the quantity d_{N_i,N_j} is calculated using the Matlab [33] function `kstest2` available in the statistics toolbox. The function output `KSSTAT` is precisely d_{N_i,N_j}.

DOI: 10.1002/nme

scaling analysis can give an estimate of the growth rate of the sample size with mesh refinement. If the distance between CDFs converges with order h^{β}, then for a refined mesh size h the sample size will scale as

$$\frac{N}{N_0}=\left(\frac{h_0}{h}\right)^{2\beta}, \tag{24}$$

where N_0 represents the acceptable sample size for mesh size h_0. For a linear convergence rate, $\beta=1$, then the sample size should increase at a rate of $2\beta=2$. If the mesh size is reduced by $1/2$, then, according to Equation (24), the sample size should increase by a factor of 4. For a quadratic convergence rate, $\beta=2$, then the sample size should increase at a rate of $2\beta=4$. If the mesh size is reduced by $1/2$, then the sample size should increase by a factor of 16.

5. EXAMPLE: CHAOTIC LOGISTIC MAP

As a first example, consider the logistic map defined by

$$L(x)=ax(1-x), \quad x\in\mathbb{R}, \tag{25}$$

where a is a real-valued parameter. The logistic map is a one degree-of-freedom discrete-time *deterministic* dynamical system. A trajectory is obtained by starting with an initial condition $x_0\in[0,1]$ and letting $x_1=L(x_0)$, $x_2=L(x_1)$, etc. The computational simplicity of the logistic map allows for the simulation of a large number of discretization levels and sample sizes.

Despite its apparent simplicity, the logistic map exhibits complex dynamical and statistical behavior. It has been extensively studied and is well characterized [34–36]. Some of the well-known dynamical and statistical properties are briefly reviewed. Let $a=4$ so that L maps the interval $[0,1]$ onto itself as shown in Figure 6(a). For this case, L is chaotic, and there are a dense set of trajectories that are extremely sensitive to initial conditions [35]. Figure 6(b) demonstrates this sensitivity to initial conditions. An initially localized set of trajectories quickly expands, filling the domain. Figure 7(a) shows two trajectories with slightly different initial conditions, $x_0=0.1$ and $x_0=0.1000001$. The two trajectories become noticeably different after 20 iterations. Figure 7(b) gives the relative frequency histogram of the logistic map after 100 iterations using an ensemble of 10^4 trajectories with initial conditions x_0 drawn from the interval $[0,1]$ with uniform probability. Note that it is more probable that a trajectory will be located near $x=0$ and $x=1$ than near $x=0.5$. The exact probability density can be obtained by using the Frobenius–Perron operator which governs the evolution of probability densities under such maps [35]. For the logistic map, any initial probability density $f_0(x)$ (of initial conditions) converges rapidly to the unique invariant probability density $f_*(x)$ given by

$$f_*(x)=\frac{1}{\pi\sqrt{x(1-x)}}. \tag{26}$$

This probability density is shown in Figure 8(a) which may be compared with the results of Figure 7(b). The CDF of Equation (26) is given by

$$F_*(x)=\frac{2}{\pi}\arctan\sqrt{\frac{x}{1-x}}. \tag{27}$$

This CDF is shown in Figure 8(b).

Now consider the following piecewise-linear approximation (or mesh) of $L(x)$

$$L_h(x)=L(x_{i-1})+\frac{L(x_i)-L(x_{i-1})}{x_i-x_{i-1}}(x-x_{i-1}), \quad x\in[x_i,x_{i-1}], \quad i=1,\ldots,n \tag{28}$$

with $h=\max(x_i-x_{i-1},\ i=1,\ldots,n)$. Examples of this approximation are shown in Figure 9. The map $L_{0.5}$ is simply the 'tent' map which is also known to be chaotic on a dense set of trajectories

DOI: 10.1002/nme

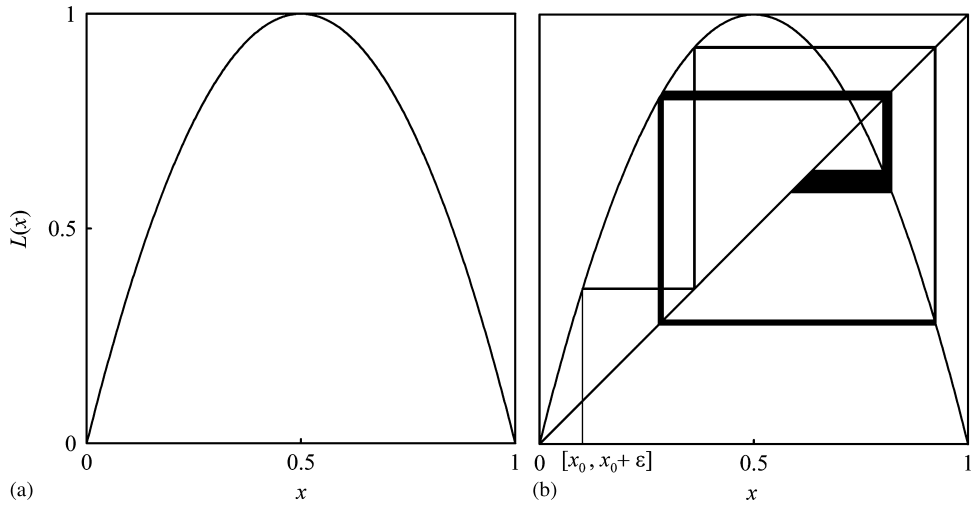

Figure 6. (a) Logistic map $L(x)=4x(1-x)$ and (b) an initially localized set of trajectories with initial conditions in the interval $[x_0, x_0+\varepsilon]$ quickly expands demonstrating sensitivity to initial conditions, a necessary condition for chaotic behavior. Here, $x_0=0.1$ and $\varepsilon=0.001$.

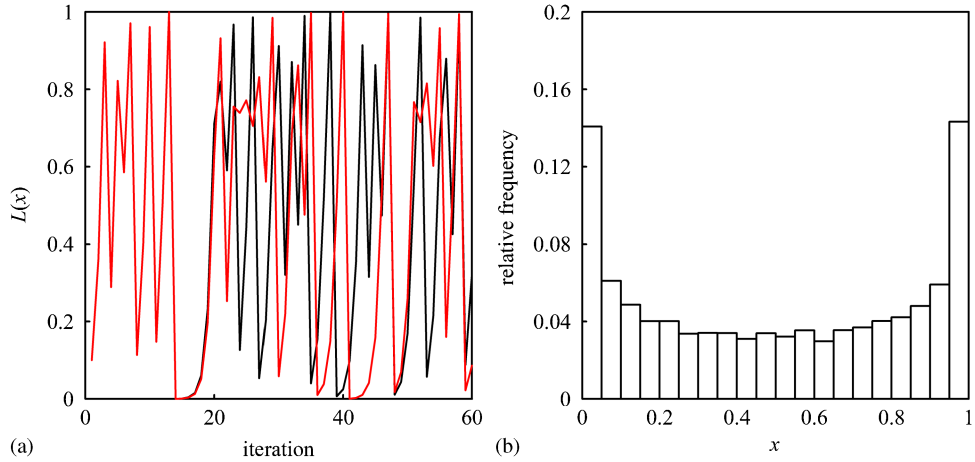

Figure 7. (a) Two trajectories of the logistic map with initial conditions $x_0=0.1$ and $x_0=0.1000001$ demonstrating sensitivity to initial conditions. The two trajectories become noticeably different after 20 iterations and (b) relative frequency histogram of the logistic map after 100 iterations (x_{100}) using an ensemble of 10^4 trajectories.

similar to the logistic map [37]. However, the probabilistic properties of the tent map are quite different from those of the logistic map. The invariant probability density of the tent map is simply the uniform density as shown in Figure 8 (as $L_{0.5}(x)$). The invariant density of the logistic map has singularities at $x=0$ and $x=1$, whereas the invariant density of the tent map is everywhere finite. Consider then the following question. Does the invariant density of $L_h(x)$ converge to that of $L(x)$ as $h\to 0$? The convergence behavior of a sequence of invariant probability densities could be studied by using the Frobenius–Perron operator to obtain the exact invariant density for each L_h. The authors, however, are not aware of such a study. In order to demonstrate the proposed method for verifying convergence in distribution, the statistics of these operators are instead studied numerically.

The results to follow use Monte Carlo sampling (initial conditions x_0 drawn from the unit interval $[0, 1]$ with uniform probability) and 100 iterations (x_{100}) of the given map. Owing to the computational simplicity of the logistic map and its discrete approximations, it is possible to

DOI: 10.1002/nme

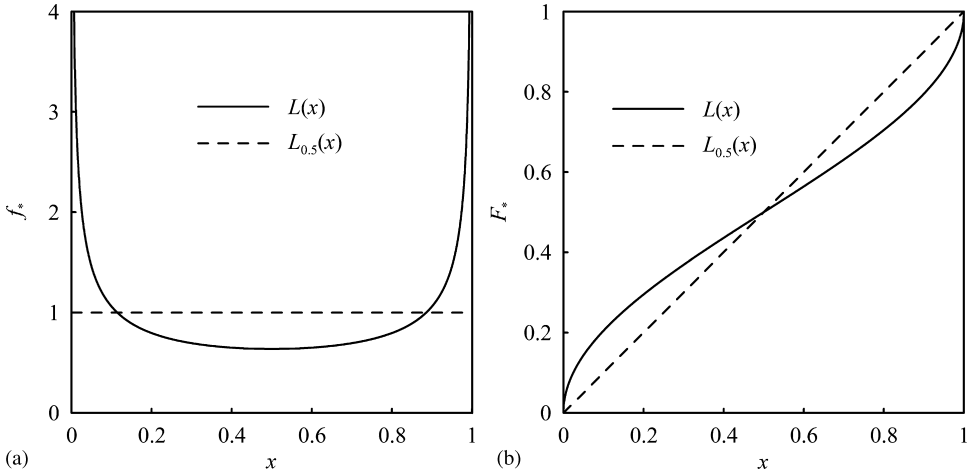

Figure 8. (a) Invariant probability density f_* of the logistic map given by Equation (26) and the tent map ($L_{0.5}$) shown in Figure 9 and (b) cumulative distribution functions.

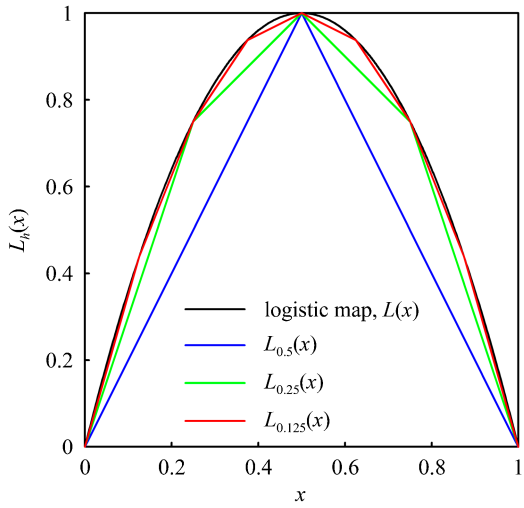

Figure 9. Piecewise-linear approximations $L_h(x)$ to the logistic map $L(x)$. $L_{0.5}$ is the 'tent' map.

run very large sample sizes. To get a sense of the sample sizes needed to assess convergence in distribution, the results from the logistic map with sample sizes $N=10^2$ and $N=10^4$ are shown in Figure 10. The exact CDF of the logistic map given by Equation (27) and tent map are shown for comparison. The $N=10^4$ sample is the same as that used in Figure 7(b) and is virtually indistinguishable from the exact CDF. For the $N=10^2$ sample the KS statistic is only about $1/2$ that of the KS statistic between the CDF of $L(x)$ and $L_{0.5}(x)$. This gives a rough idea of the sample sizes needed to investigate the convergence behavior of $L_h(x)$ as $h\to 0$.

Consider now a sequence of discretizations, $h=(1/2)^i,\ i=2,\ldots,10$, and a sequence of sample sizes, $N=10^j,\ j=2,\ldots,6$. Since the converged CDF is known (Equation (26)), the discretization and sampling error can be assessed directly instead of using pairwise differences. The confidence bound given in Equation (19) then reduces to one term. Figure 11(a) shows the resulting error norm for each discretization level and sample size but without confidence bounds. Figure 11(b)–(f) gives the same results but with 95% confidence bounds obtained using Equation (19). The ranges on the error bars do not appear symmetric due to the logarithmic axes. (Note that since the KS statistic is positive, the minimum value of an error bar is restricted to be greater than or equal to zero. In figures with a logarithmic scale a zero value is represented by an arrow.) Figures 11(b) and

DOI: 10.1002/nme

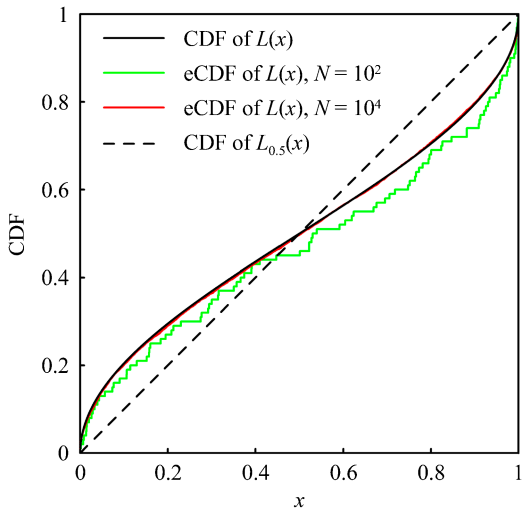

Figure 10. Two eCDFs of sample size $N = 10^2$ and $N = 10^4$ of the logistic map after 100 iterations (x_{100}). The exact (invariant) CDFs of the logistic map and tent map are shown for comparison.

(c) indicate that the 95% confidence bounds for $N = 10^2$ and $N = 10^3$ are still quite large relative to the true discretization error even at the coarsest mesh refinement levels $h = 1/4$ and $h = 1/8$. Note from Figure 11(f) that for the smallest mesh size $h = 1/1024$, even sample sizes on the order of $N = 10^6$ are insufficient to resolve the discretization error with 95% confidence. Also, note that in Figure 11(c) the 95% confidence bound for $h = 1/512$ and $N = 10^3$ does not contain the error predicted at $N = 10^6$, unlike every other mesh level and sample size. This observation reinforces the fact that there is a 5% probability that the true error will be outside the 95% confidence bound.

In practice, the converged CDF is typically unknown. Convergence can then be assessed in a Cauchy sense by examining the pairwise L_∞ distance between successive discretization levels. Figure 12 gives the pairwise L_∞ distance between successive discretization levels using the same sequence of discretizations and sample sizes used in Figure 11. The mesh size h represents the smallest mesh size of the given pair of meshes. Note that the confidence bound has been reduced from 95 to 90% as noted in the proof of Equation (19). Also, the size of the confidence bounds is roughly doubled compared with those given in Figure 11. Note that for all mesh levels the confidence bounds for sample sizes $N = 10^2$ to $N = 10^5$ bracket the pairwise differences given at $N = 10^6$.

Figures 11 and 12 indicate that the convergence rate with mesh refinement is approximately 1.0 throughout the range of mesh levels. A confidence bound on the convergence rate could be obtained by looking at the minimum and maximum values of adjacent confidence bounds. However, unless the confidence bounds are very tight this bound could be relatively large and even negative. In general, relatively large sample sizes are needed to accurately assess the convergence rate as opposed to a single pairwise difference. Optimum sampling at each mesh level is thus advantageous and is discussed in Section 7.

6. EXAMPLE: FRAGMENTING RING

As a second example the expanding ring experiments of Benson and Grady [38] are modeled using the explicit-dynamics finite element code Alegra [39]. In these experiments a thin aluminum 1100-0 ring with outer diameter 32 mm and a 1 mm × 1 mm square cross-section is expanded by electromagnetic forces and ultimately fragmented. Strain rates are on the order of $10^4/\mathrm{s}$. Because of the small cross-sectional width to diameter ratio of the ring as well as the ductile nature of aluminum 1100-0, ring fracture is precipitated by necking followed by fracture through the

DOI: 10.1002/nme

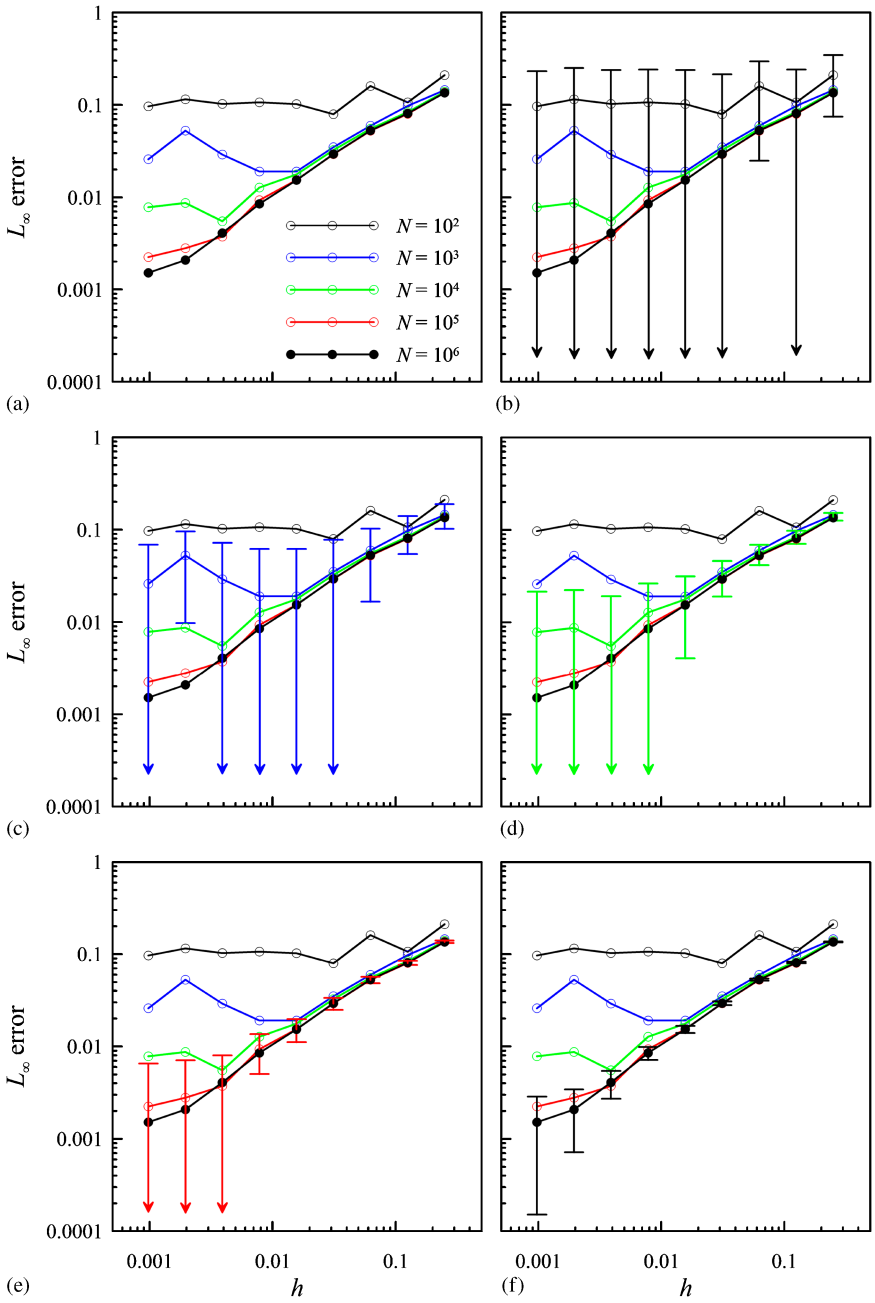

Figure 11. L_∞ error norm in the sampled CDFs obtained from piecewise-linear approximations to the logistic map for various sample sizes N as a function of mesh size h. Confidence bounds are 95%: (a) confidence bounds are not shown; (b) confidence bounds are shown for $N = 10^2$; (c) confidence bounds are shown for $N = 10^3$; (d) confidence bounds are shown for $N = 10^4$; (e) confidence bounds are shown for $N = 10^5$; and (f) confidence bounds are shown for $N = 10^6$.

cross-section. The experimentally observed necks and fracture locations are distributed unevenly with numerous unfractured necks. The existence of unfractured necks is attributed to Mott release waves [18].

It is well known that ductile fracture is preceded by material softening which can cause the governing PDEs to become ill-posed with accompanying mesh dependent (nonconvergent) results [14, 15]. Much research has been devoted to studying material softening, and a number of techniques

DOI: 10.1002/nme

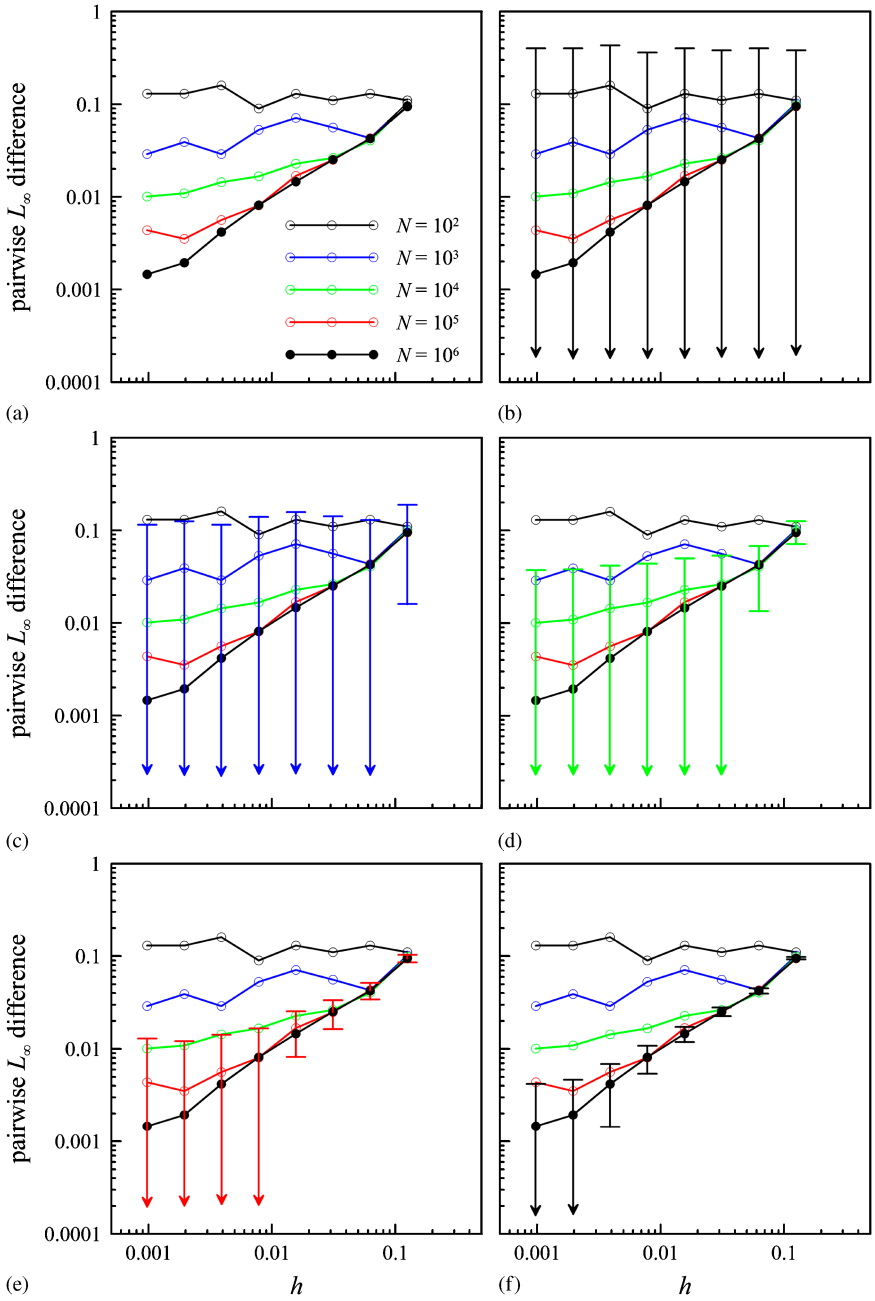

Figure 12. Pairwise L_∞ difference in the sampled CDFs obtained from piecewise-linear approximations to the logistic map for various sample sizes N as a function of mesh size h. Confidence bounds are 90%: (a) confidence bounds are not shown; (b) confidence bounds are shown for $N = 10^2$; (c) confidence bounds are shown for $N = 10^3$; (d) Confidence bounds are shown for $N = 10^4$; (e) confidence bounds are shown for $N = 10^5$; and (f) confidence bounds are shown for $N = 10^6$.

exist to regularize the governing equations, for example, by including nonlocal or rate dependent material behavior [40, 41]. For this example, since any fracture occurs at a neck but not all necks fracture, the focus here is not on the broader issue of fragment distribution convergence in the presence of material softening, but rather on the more immediate issue of convergence in neck spacing. For this reason the neck spacing statistics are analyzed before any fractures actually occur, in particular $t = 40\,\mu s$. This time threshold was chosen to be as large as possible while

DOI: 10.1002/nme

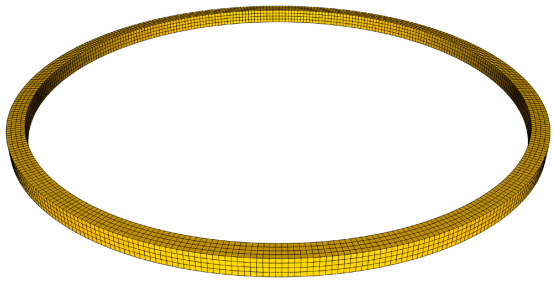

Figure 13. Ring finite element mesh with four elements through the thickness (denoted by R0) consisting of 6016 hexahedral elements. Additional mesh refinements were obtained through uniform hierarchical refinement: R1, 48 K elements; R2, 385 K elements; R3, 3.08 M elements.

assuring that the plastic strain within the necks is in the pre-softening regime and the finite element mesh distortion is still moderate. Furthermore, only necks that have reduced the cross-sectional area below a threshold of $A/A_o = 0.6$, with A_o the initial cross-section area of $1\,\text{mm}^2$, are included in the statistical analysis. The material between these critical necks is referred to as 'pre-fragments' in the subsequent discussion. Because the actual ring fracture is not modeled, direct comparisons with the experimental fragmentation statistics will not be made here. The statistical method presented in the previous sections is used to analyze the convergence of the pre-fragment distribution under hierarchical mesh refinement. Figure 13 shows the base finite element mesh (denoted by R0) consisting of four elements through the thickness and a total of 6016 hexahedral elements. Additional mesh refinements are obtained through uniform hierarchical refinement in which each element is subdivided into 8 elements resulting in mesh R1 with 48 K elements, mesh R2 with 385 K elements, and mesh R3 with 3.08 M elements.

The neck locations are generally believed to be governed by variability in initial geometrical imperfections and material properties. Several researchers have suggested seeding material properties with variability in numerical simulations to capture such effects (e.g. [42–44]). For this example, the initial yield stress is perturbed. Two different random field representations of the initial yield stress are considered: (1) a random field with spatial correlation obtained through a method based on the Hilbert space-filling curve (discussed below) with each resulting cell treated as independent and identically distributed and (2) a random field with no spatial correlation in which each finite element is treated as independent and identically distributed. The inelastic behavior of the aluminum is modeled using the Johnson–Cook [45] plasticity model with isotropic hardening. The thermal dependence and strain rate dependence are turned off leaving only the power-law hardening term

$$\sigma = \sigma_{\text{yield}} + H\varepsilon_p^n, \tag{29}$$

where σ is the Von Mises flow stress, ε_p is the equivalent plastic strain, H is the hardening modulus, n is the hardening exponent, and σ_{yield} is the initial yield stress. Here, $n = 0.34$, $H = 20\,\text{MPa}$, and the distribution for σ_{yield} is given by the Weibull probability density function (Equation (4)) with a median value of 80 MPa and Weibull modulus (shape parameter) $\eta = 25$ (the scale parameter $\gamma = \text{median}(\sigma_{\text{yield}})/(\ln 2)^{1/\eta} = 78.8357$). This distribution is shown in Figure 14.

Alegra has the option of letting any material parameter vary spatially based on an iterate of the Hilbert space-filling curve [46]. A space-filling curve is a continuous mapping $\mathbf{x}: \mathbb{R} \to \mathbb{R}^3$ from the open unit interval on the real line onto a higher dimensional region such as a cube. The continuity properties of the space-filling curve imply that $\|\mathbf{x}(r) - \mathbf{x}(s)\| < a|r - s|$ for some constant a [46]. Thus, if r and s are close together, then their image is guaranteed to be close as well. However, the reverse is not true. The space-filling algorithm in Alegra creates irregularly shaped cells or aggregates of a specified size, and thus introduces a new length scale in the problem. Note that the Hilbert space-filling curve is not a physics-based spatial correlation model but is merely a numerically expedient method for introducing variability based on a user specified correlation distance. For this example, the aggregate size is taken to be 1/4 of the ring

DOI: 10.1002/nme

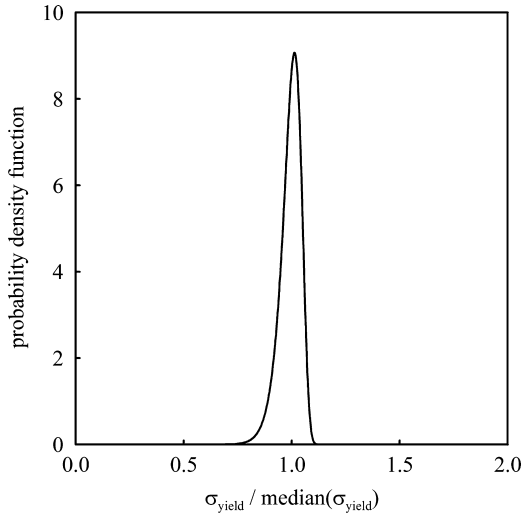

Figure 14. Weibull probability density function for the initial yield stress with Weibull modulus $\eta = 25$.

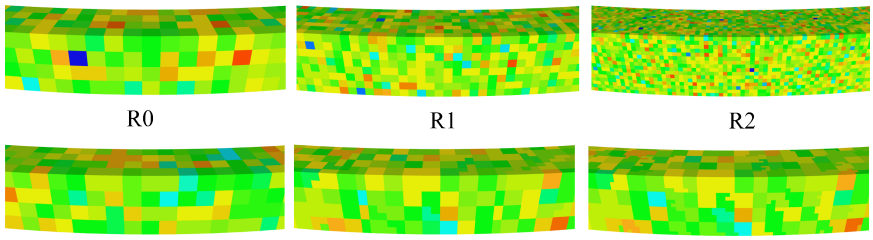

Figure 15. Zoomed-in views of realizations of the initial yield stress for mesh refinements R0, R1, and R2. The top row is the *uncorrelated* random field case in which each *element* is independent and identically distributed with distribution shown in Figure 14. The bottom row is the *correlated* random field case in which the initial yield stress is obtained from the Hilbert space-filling curve and each *cell* is independent and identically distributed with distribution shown in Figure 14 (red $\sim \sigma_{\text{yield}}/\text{median}(\sigma_{\text{yield}}) > 1.125$, blue $\sim \sigma_{\text{yield}}/\text{median}(\sigma_{\text{yield}}) < 0.75$).

cross-sectional width, namely 0.25 mm. Note that all mesh resolutions used in this example, R0–R4, resolve this length scale. Each aggregate is idealized as homogeneous and isotropic. Before each simulation a randomly oriented coordinate transformation is applied to the finite element mesh in order to remove the coordinate system bias in the space-filling curve algorithm. Zoomed-in views of realizations of both the uncorrelated and correlated initial yield stress are shown in Figure 15 for mesh refinements R0, R1, and R2. For the uncorrelated case, the stochastic dimension is equal to the number of elements in the finite element mesh, and is therefore dependent on the mesh refinement level. For the correlated case, the stochastic dimension is approximately equal to the number of elements in the base mesh R0 (~ 6000).

Instead of simulating the actual electromagnetic loading on the ring, a pressure step input of 50 MPa is applied for 10 μs on the inner radius. The deformed state of the ring at $t = 40\,\mu$s for a correlated random field realization is shown in Figure 16. The color represents the equivalent plastic strain. Note the various stages of neck formation. In all simulations there was no significant visual difference between deformed rings using either the correlated or uncorrelated random field realizations. The cross-sectional area of the deformed ring was extracted using the coordinated system shown in Figure 17. The postprocessing software Paraview [47] was used to extract the cross-sectional area as a function of circumferential angle, $A(\theta)$, by using cutting planes on the deformed

DOI: 10.1002/nme

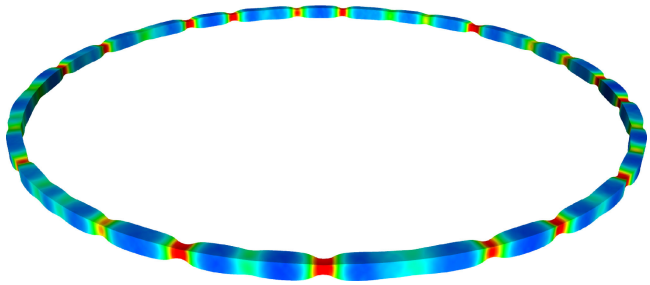

Figure 16. Deformed state of the expanding ring with color representing equivalent plastic strain (red>50%), $t = 40\,\mu$s. Note the various stages of neck formation.

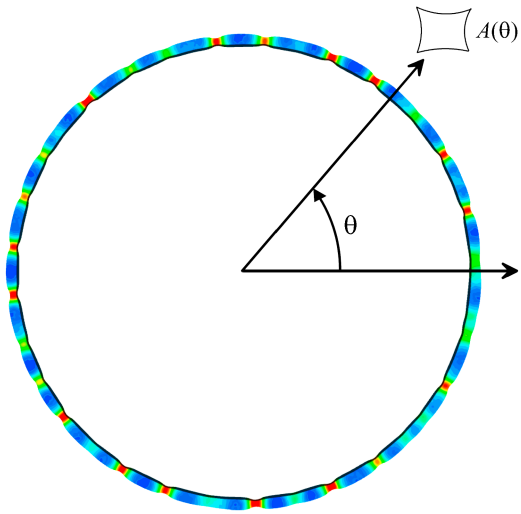

Figure 17. Ring coordinate system used in extracting the radial cross-sectional area $A(\theta)$.

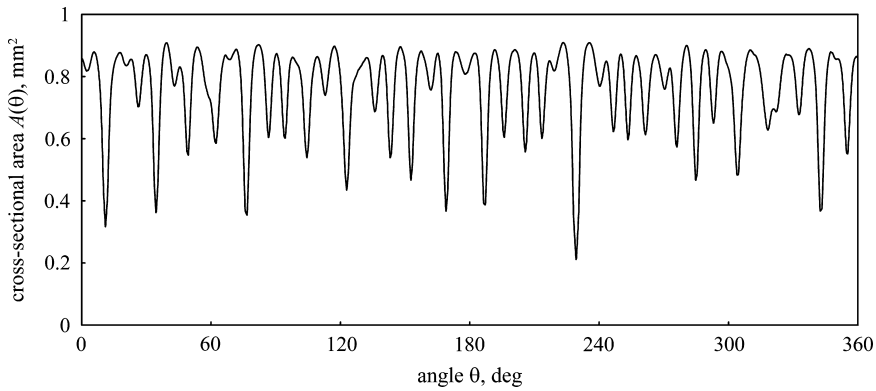

Figure 18. Extracted ring cross-sectional area $A(\theta)$ at $t = 40\,\mu$s.

mesh. For all mesh refinement levels, at least four cutting planes were used per representative element size. An extracted cross-sectional area curve is shown in Figure 18. All relative minima with values below the area threshold of 0.6 mm were extracted and identified as critical necks. The material between two neighboring critical necks was identified as a pre-fragment.

The Monte Carlo sampling consisted of 100 simulations at each mesh refinement level, R0–R4. The R0 and R1 mesh refinement simulations were performed using a single CPU, whereas

DOI: 10.1002/nme

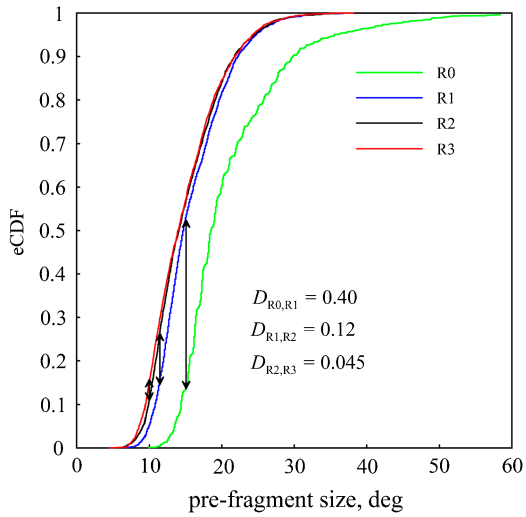

Figure 19. Cumulative distribution functions of the pre-fragment size for the four mesh refinement levels, R0-R4, *with* spatial correlation in initial yield stress. The results are combined from a Monte Carlo ensemble of size 100 for each mesh level. Ensemble pre-fragment sample sizes are $N_{R0}=1714$, $N_{R1}=2274$, $N_{R2}=2386$, $N_{R3}=2421$. The pairwise L_∞ differences are also shown (cf. Figure 20).

the R2 and R3 refinement simulations were performed with 16 and 128 CPUs, respectively. For each simulation the random fields were generated using a unique random seed. Figure 19 shows the eCDF of the combined pre-fragment statistics for each mesh refinement level for the spatially *correlated* random field. The pairwise L_∞ differences are also shown. The ensemble pre-fragment sample sizes are $N_{R0}=1714$, $N_{R1}=2274$, $N_{R2}=2386$, $N_{R3}=2421$. Figure 20 shows the eCDF of the combined pre-fragment statistics for each mesh refinement level for the spatially *uncorrelated* random field. The ensemble pre-fragment sample sizes are $N_{R0}=1686$, $N_{R1}=2424$, $N_{R2}=2766$, $N_{R3}=2905$. Note the stair-step patterns in the pre-fragment eCDFs for the R0 mesh refinement in both Figures 19 and 20. This pattern is the result of the quantization effect described in Section 3.2. The distance between necks is quantized by the finite element mesh, since the area minima shown in Figure 18 can only occur at the finite element interfaces. This quantization effect is not visually noticeable in the other mesh refinements but is still present.

The pairwise L_∞ differences are shown in Figure 21(a) and (b) for the spatially *correlated* and *uncorrelated* random fields, respectively, as a function of finite element size (minimum in pair). The red error bars represent the sampling error (90% confidence, Equation (19)), and the additional blue error bars represent the quantization error (Equation (17)). Note that the quantization error decreases with mesh size. These same results are combined in Figure 22 but with logarithmic axes. Estimated convergence rates in the L_∞ norm are given as 1.4 for the spatially correlated case and 0.86 for the spatially uncorrelated case. The spatially uncorrelated case still gives an indication of convergence, albeit with a reduced rate compared with the spatially correlated case. Also, note by comparing Figure 19 with Figure 20 that the two cases converge to different distributions.

Note that all the pre-fragments generated for a given mesh size were collected and used in the eCDFs of Figures 19 and 20. As discussed in Section 3.1 this is a form of cluster sampling and should be used with caution when the statistical method is based on simple random sampling [31]. Using the adjusted population correlation coefficient given by Equations (14)–(16) for this example results in $R_a^2 \approx 10^{-2}$ for each mesh refinement level. Since this value is close to zero the cluster sampling used in this example is a good approximation to a simple random sample, and therefore the use of the KS statistic is justified.

DOI: 10.1002/nme

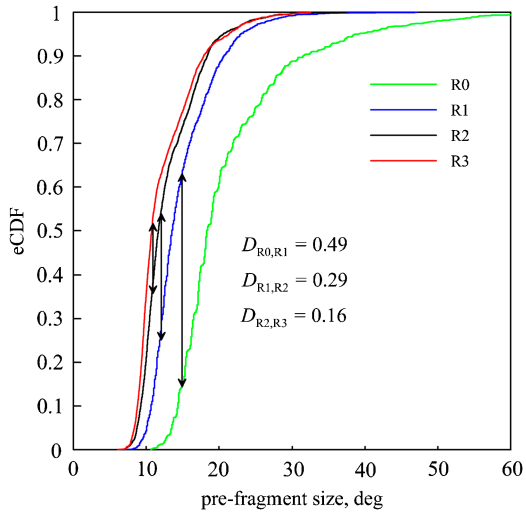

Figure 20. Cumulative distribution functions of the pre-fragment size for the four mesh refinement levels, R0-R4, *without* spatial correlation in initial yield stress. The results are combined from a Monte Carlo ensemble of size 100 for each mesh level. Ensemble pre-fragment sample sizes are $N_{R0}=1686$, $N_{R1}=2424$, $N_{R2}=2766$, $N_{R3}=2905$. The pairwise L_∞ differences are also shown (cf. Figure 19).

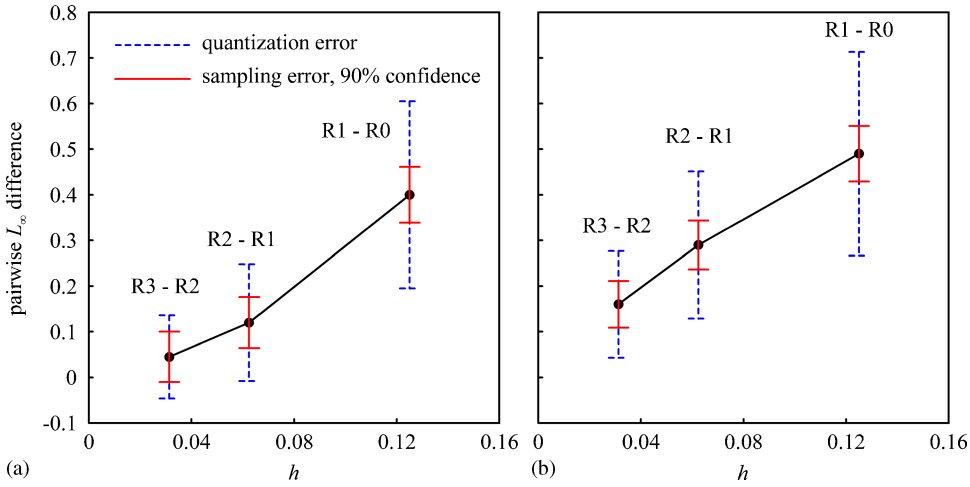

Figure 21. Pairwise L_∞ differences as a function of mesh size for both the: (a) spatially correlated and (b) spatially uncorrelated initial yield stress field. Error bars are given for both the sampling error (90% confidence) and the quantization error.

7. OPTIMUM SAMPLE SIZES

The main challenge in verifying convergence in distribution using Monte Carlo sampling is the large sample sizes required. It is therefore critical to use only the minimum required sample size at each mesh refinement level to resolve the pairwise L_∞ distance between two mesh levels. This set of minimum sample sizes can be obtained using a simulation cost function, an assumed convergence rate, and a specified relative sampling accuracy. For the cost function, suppose for simplicity that each simulation for a given mesh produces one sample of the output variable. The cost of running an ensemble of simulations at a given mesh refinement level is then directly

DOI: 10.1002/nme

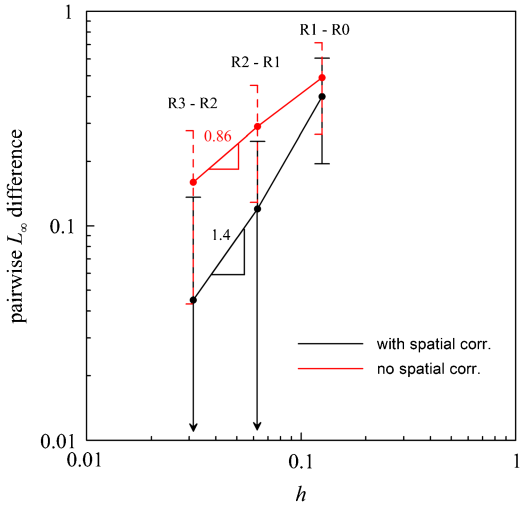

Figure 22. Pairwise L_∞ differences as a function of mesh size for both the spatially correlated and uncorrelated initial yield stress field. Error bars represent the sum of the sampling error (90% confidence bounds) and the quantization error. Estimated convergence rates are shown.

proportional to the number of samples. A reasonable cost function F_c for a sequence of n meshes is given by

$$F_c(N_1, N_2, \ldots, N_n) := a_1 N_1 + a_2 N_2 + \cdots + a_n N_n. \tag{30}$$

The coefficients a_i may be determined by running at least one simulation at each mesh refinement level and determining the subjective cost (e.g. computation time, mesh size, computer memory used) of a simulation at each mesh refinement level relative to the base level. Only the ratios of the coefficients are needed, for example, $a_2 = 4a_1$, $a_3 = 16a_1$, etc. The optimization problem is then to minimize the cost function F_c subject to constraints on the sampling accuracy between each successive pair of mesh refinement levels. Let the relative sampling accuracy be denoted by δ. Using Equation (23) the relative accuracy constraint C_i between mesh levels i and $i+1$ is given by

$$C_i(N_i, N_{i+1}) := \frac{z_i/\sqrt{N_i} + z_{i+1}/\sqrt{N_{i+1}}}{d_{i,i+1}} - \delta = 0, \quad i = 1, \ldots, n-1. \tag{31}$$

The true distances $d_{i,i+1}$ are of course unknown and are only estimated via $d_{N_i,N_{i+1}}$ as the ensemble sampling progresses. However, the $d_{i,i+1}$ can be estimated *a priori* if $d_{1,2}$ is known and one assumes a convergence rate β.

The constrained minimization problem given by Equations (30) and (31) may be solved using the technique of Lagrange multipliers [48]. The augmented Lagrangian L_A associated with the constrained problem is defined as

$$L_A(N_1, \ldots, N_n, \lambda_1, \ldots, \lambda_{n-1}) := F_c(N_i) + \lambda_1 C_1 + \cdots + \lambda_{n-1} C_{n-1}, \tag{32}$$

where λ_i, $i = 1, \ldots, n-1$ are the Lagrange multipliers. The necessary conditions for a local minimum of the constrained problem are given by

$$\frac{\partial L_A}{\partial N_i} = 0, \quad i = 1, \ldots, n. \tag{33}$$

DOI: 10.1002/nme

Substituting Equation (32) into Equation (33) yields

$$\begin{aligned} N_1 &= \left(\frac{\lambda_1 z_1}{2a_1}\right)^{2/3}, \\ N_2 &= \left(\frac{(\lambda_1+\lambda_2) z_2}{2a_2}\right)^{2/3}, \\ N_3 &= \left(\frac{(\lambda_2+\lambda_3) z_3}{2a_3}\right)^{2/3}, \\ &\vdots \\ N_{n-1} &= \left(\frac{(\lambda_{n-2}+\lambda_{n-1}) z_{n-1}}{2a_{n-1}}\right)^{2/3}, \\ N_n &= \left(\frac{\lambda_{n-1} z_n}{2a_n}\right)^{2/3}. \end{aligned} \tag{34}$$

Substituting Equation (34) into the constraint equations given in Equation (31) gives

$$\begin{aligned} \left(\frac{\lambda_1}{2a_1 z_1}\right)^{-1/3} + \left(\frac{\lambda_1+\lambda_2}{2a_2 z_2}\right)^{-1/3} &= \delta d_{1,2}, \\ \left(\frac{\lambda_1+\lambda_2}{2a_2 z_2}\right)^{-1/3} + \left(\frac{\lambda_2+\lambda_3}{2a_3 z_3}\right)^{-1/3} &= \delta d_{2,3}, \\ &\vdots \\ \left(\frac{\lambda_{n-3}+\lambda_{n-2}}{2a_{n-2} z_{n-2}}\right)^{-1/3} + \left(\frac{\lambda_{n-2}+\lambda_{n-1}}{2a_{n-1} z_{n-1}}\right)^{-1/3} &= \delta d_{n-2,n-1}, \\ \left(\frac{\lambda_{n-2}+\lambda_{n-1}}{2a_{n-1} z_{n-1}}\right)^{-1/3} + \left(\frac{\lambda_{n-1}}{2a_n z_n}\right)^{-1/3} &= \delta d_{n-1,n}. \end{aligned} \tag{35}$$

These are $n-1$ non-linear equations for the $n-1$ Lagrange multipliers. The banded structure of the equations can be exploited to analytically obtain a single non-linear equation in one unknown. Given a numerical solution to this single non-linear equation, subsequent back substitution gives the solution for the remaining Lagrange multipliers. Once the Lagrange multipliers are known, the sample sizes can be obtained from Equation (34). Sufficient conditions for critical points to be local minima are given in Lueberger [48] based on the Hessian matrix of L_{A}. For the present case the Hessian matrix of L_{A} is positive definite for all values of N_i. Therefore, the critical points are indeed global minima.

The case of only two meshes, $n=2$, can be solved analytically. The optimum sample sizes N_1 and N_2 are given by

$$N_1 = \frac{(z_1/2a_1)^{2/3}}{(\delta d_{1,2})^2}[(2a_1 z_1)^{2/3} + (2a_2 z_2)^{2/3}]^3, \tag{36}$$

$$N_2 = \frac{(z_2/2a_2)^{2/3}}{(\delta d_{1,2})^2}[(2a_1 z_1)^{2/3} + (2a_2 z_2)^{2/3}]^3. \tag{37}$$

Note that $N_2/N_1 = (z_2 a_1/z_1 a_2)^{2/3}$, and if $z_1 = z_2$ then $N_2/N_1 = (a_1/a_2)^{2/3}$. As expected for equal costs, $a_2 = a_1$, then $N_2 = N_1$. If the second mesh is eight times more expensive than the first ($a_2 = 8a_1$), then $N_2 = 4N_1$. Also, note that Equations (36) and (37) are invariant under the substitution $\delta d_{1,2} \to c\delta d_{1,2}$, $N_i \to c^{-2} N_i, i = 1, 2$. Thus, once the optimum sample sizes are found for a given value of the product $\delta d_{1,2}$, the optimum sample sizes can be found for any other value of $\delta d_{1,2}$.

DOI: 10.1002/nme

Table I. Optimum sample sizes for the cost function $F_c = N_1 + N_2 + N_3 + \cdots$ and linear convergence rate ($\beta = 1$) ($d_{1,2} = 0.4$, $\delta = 0.5$, $z_i = 1.36$).

n	N_1	N_2	N_3	N_4	N_5	N_6
2	185	185				
3	82	750	731			
4	119	328	2989	2932		
5	98	475	1311	11956	11722	
6	108	391	1898	5244	47819	46889

Table II. Optimum sample sizes for the cost function $F_c = N_1 + 2N_2 + 4N_3 + \cdots$ and linear convergence rate ($\beta = 1$) ($d_{1,2} = 0.4$, $\delta = 0.5$, $z_i = 1.36$).

n	N_1	N_2	N_3	N_4	N_5	N_6
2	237	149				
3	77	949	594			
4	125	305	3793	2374		
5	96	497	1219	15171	9494	
6	109	384	1986	4875	60683	37974

Table III. Optimum sample sizes for the cost function $F_c = N_1 + 4N_2 + 16N_3 + \cdots$ and linear convergence rate ($\beta = 1$) ($d_{1,2} = 0.4$, $\delta = 0.5$, $z_i = 1.36$).

n	N_1	N_2	N_3	N_4	N_5	N_6
2	310	123				
3	72	1240	491			
4	130	285	4960	1964		
5	94	520	1137	19838	7856	
6	110	376	2079	4546	79351	31424

Table IV. Optimum sample sizes for the cost function $F_c = N_1 + 8N_2 + 64N_3 + \cdots$ and linear convergence rate ($\beta = 1$) ($d_{1,2} = 0.4$, $\delta = 0.5$, $z_i = 1.36$).

n	N_1	N_2	N_3	N_4	N_5	N_6
2	417	105				
3	67	1666	417			
4	136	267	6662	1665		
5	93	544	1066	26646	6658	
6	111	369	2175	4262	106583	26629

In particular, if $\delta d_{1,2}$ is reduced by a factor of two, then N_1 and N_2 are increased by a factor of four. This scaling result holds for the general case as well

$$\begin{aligned} \delta d_{i,i+1} &\to c\delta d_{i,i+1}, \quad i = 1, 2, \ldots, n-1, \\ N_i &\to c^{-2} N_i, \quad i = 1, n. \end{aligned} \tag{38}$$

The optimum sample sizes are given in Tables I–IV for the linear cost functions $F_c = N_1 + N_2 + N_3 + \cdots$, $F_c = N_1 + 2N_2 + 4N_3 + \cdots$, $F_c = N_1 + 4N_2 + 16N_3 + \cdots$, and $F_c = N_1 + 8N_2 + 64N_3 + \cdots$, respectively, with $d_{1,2} = 0.4$, $\delta = 0.5$, a 95% confidence level ($z_i = 1.36$), and a linear convergence rate ($\beta = 1$). These values are also plotted in Figure 23. Note that these cost functions mainly affect the sample sizes near the end of the mesh sequence, in particular the last two, with only minor perturbations on the earlier values of the sequence. In general, the sample size of the last mesh in the sequence is reduced at the expense of the sample size of the second to last mesh. The optimum

DOI: 10.1002/nme

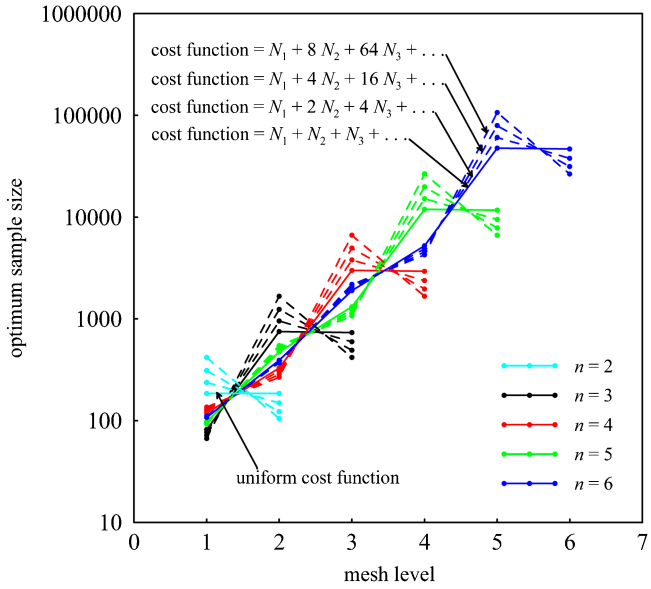

Figure 23. Optimum sample sizes for a sequence of n meshes and various cost functions ($\beta = 1, d_{1,2} = 0.4, \delta = 0.5$). The optimum sample sizes for different values of δ and $d_{1,2}$ can be obtained by using the scaling relation in Equation (38).

sample sizes for different values of δ and $d_{1,2}$ can be obtained by using the scaling relation in Equation (38).

For an example application of this optimization method the logistic map given in Section 5 is used. For this relatively simple system, the cost per simulation is to a first approximation independent of the mesh size. The mesh sequence has length $n = 9$ so the cost function is $F_c = N_1 + N_2 + \cdots + N_9$. As discussed at the end of Section 5, the convergence rate is approximately linear ($\beta \approx 1$). From Figure 12 $d_{1,2} \approx 0.1$. (Of course, this information would not normally be known *a priori*.) Taking the sampling accuracy $\delta = 0.5$ and $z_i = 1.36$, solving Equation (35) for the Lagrange multipliers, and substituting into Equation (34) yields the following the sample sizes: $N_i = 1660$, 6710, 26 200, 110×10^3, 400×10^3, 1.94×10^6, 5.37×10^6, 49.0×10^6, 48.0×10^6. The results from simulations using these sample sizes are shown in Figure 24(b). The uniform sampling results shown in Figure 12(f) are shown again in Figure 24(a) for comparison. Since the assumed convergence rate of $\beta = 1$ is fairly accurate for this example, the relative size of the confidence bands is nearly constant as desired. In practice when the convergence rate is unknown, the updated values $d_{N_i, N_{i+1}}$ could be used to obtain new estimates of the true optimal sample sizes in an iterative manner.

8. CONCLUSIONS

One necessary condition for verification is that numerical approximations converge with discretization refinement. A method was presented for verifying mesh convergence in a sequence of statistical distributions generated by direct Monte Carlo sampling. The primary application of this method is to assess the mesh or grid convergence, and possibly divergence, of stochastic outputs from non-linear continuum systems, for example from fluid or solid mechanics, particularly those with instabilities and sensitive dependence on initial conditions or system parameters. The method verifies convergence in distribution using the L_∞ norm in the space of continuous CDFs. The effect of finite sample sizes is quantified using confidence levels from the KS statistic. The method is independent of the particular form of the underlying distributions, and only assumes that they are continuous. An empirical demonstration of convergence is, however, only one step in the

DOI: 10.1002/nme

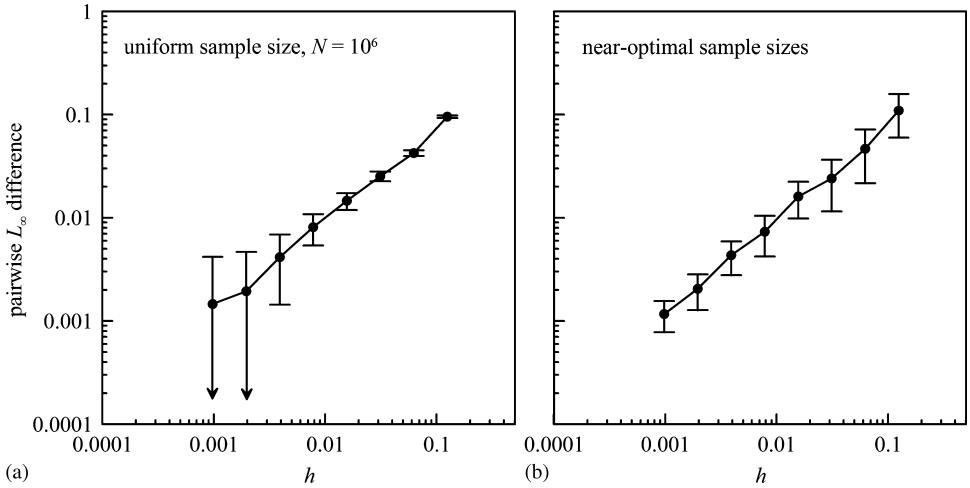

Figure 24. Pairwise L_∞ difference in sampled CDFs obtained from piecewise-linear approximations to the logistic map as a function of mesh size h: (a) uniform sample size $N = 10^6$ and (b) near-optimal sampling using the method given in Section 7. The 90% confidence bounds are shown.

verification process. A broader task is verifying that the converged distribution is a unique solution of the original mathematical model.

The statistical method was demonstrated using two examples: (1) the logistic map in the chaotic regime, and (2) a fragmenting ductile ring modeled with an explicit-dynamics finite element code. In the first example, the logistic map was discretized with piecewise-linear approximations. Using Monte Carlo sampling, the sequence of invariant distributions corresponding to the each piecewise-linear approximation was shown to converge in distribution to the invariant distribution of the logistic map. For the expanding ring example, the convergence of the distribution describing neck spacing was investigated for two different random field representations of the initial yield stress, one with spatial correlation and the other without. Both cases converged albeit to different distributions. The case with spatial correlation exhibited a significantly higher convergence rate compared with the one without spatial correlation.

The main challenge in applying the presented statistical method is the relatively large samples sizes required. This issue is common to Monte Carlo methods in general. To partially address this issue an optimization problem was formulated to obtain minimum sample sizes at each mesh refinement level for a given mesh convergence rate and constraints on sampling accuracy. This constrained optimization problem was solved using Lagrange multipliers, and demonstrated using the first example. Tables of sample sizes were given for several cost functions and convergence rates. Even with this minimization technique the number of required simulations is admittedly quite large, especially at higher mesh refinement levels where the computational cost is the greatest.

While the presented method used the L_∞ norm and the associated KS statistic, other distance functions and their associated statistics could be explored as well, for example using the L_1 and L_2 norms. The use of the L_1 norm has been proposed by Roy and Oberkampf [19, 20] for use in model validation. The use of these other norms might allow for a convergence assessment of discontinuous CDFs, and they would be less sensitive to the steepness of the CDF (see Figure 20). The required sample sizes for equivalent confidence bounds in these norms may be smaller than those for the L_∞ norm, although the $O(1/\sqrt{N})$ scaling in the confidence bounds would be the same. At first thought, an assessment of mesh convergence in only the mean or variance of an engineering quantity of interest would seemingly require smaller sample sizes. However, the confidence bound on the mean has the same $O(1/\sqrt{N})$ scaling and is additionally proportional to the standard deviation [29, p. 43]. One can envision examples in which the mean converged with mesh refinement but the standard deviation diverged, or that the standard deviation had a slower convergence rate than the mean. Thus, statements of relative sampling efficiencies are expected to

DOI: 10.1002/nme

be problem dependent and require further assumptions on the underlying distribution. Our future research will focus on investigating these questions.

Finally, although this paper has focused on verification, once numerical simulations have been verified to converge, the KS statistic could also be used as a validation tool in a manner analogous to its conventional use in hypothesis testing [21, 3 13.9]. Given both a sample set from experiments and a sample set from numerical simulations, the two-sample KS test [21, p. 485] provides a probability (confidence) that the two sample sets are from the same distribution.

ACKNOWLEDGEMENTS

The comments and suggestions from the reviewers of this paper greatly improved the quality of the paper and are gratefully acknowledged. Funding for this research was provided by the U.S. Department of Energy's Advanced Simulation and Computing (ASC) program, the Project Manager for the Heavy Brigade Combat Team (PM HBCT, Mr John Rowe), and the Army Research Laboratory (under Sandia National Laboratories WFO Proposal Number 014081218), and is gratefully acknowledged. Partial funding for the first author also includes the Defense Threat Reduction Agency (prime award HDTRA1-09-0029 to Rensselaer Polytechnic Institute, subcontract A12051 to Sandia National Laboratories). The research presented in Section 7 was funded by the Center for Frontiers of Subsurface Energy Security (an Energy Frontier Research Center funded by the U.S. Department of Energy, Office of Science, Office of Basic Energy Sciences under Award Number DE-SC0001114), and is gratefully acknowledged. Sandia National Laboratories is a multi-program laboratory operated by Sandia Corporation, a wholly owned subsidiary of Lockheed Martin Corporation, for the U.S. Department of Energy's National Nuclear Security Administration under contract DE-AC04-94AL85000.

REFERENCES

1. AIAA. Guide for the verification and validation of computational fluid dynamics simulations. American Institute of Aeronautics and Astronautics, AIAA-G-077-1998: Reston, VA, 1998.
2. ASME. Guide for verification and validation in computational solid mechanics. American Society of Mechanical Engineers, ASME Standard V&V 10-2006: New York, NY, 2006.
3. Roache P. *Verification and Validation in Computational Science and Engineering*. Hermosa Publishers: Albuquerque, New Mexico, 1998.
4. Oberkampf W, Trucano T, Hirsch C. Verification, validation, and predictive capability in computational engineering and physics. *Applied Mechanics Reviews* 2004; **57**(5):345–384.
5. Meulbroek J, Ramesh K, Swaminathan P, Lennon A. CTH simulations of an expanding ring to study fragmentation. *International Journal of Impact Engineering* 2008; **35**(12):1661–1665.
6. Schuëller G, Pradlwarter H. Uncertainty analysis of complex structural systems. *International Journal for Numerical Methods in Engineering* 2009; **80**:881–913.
7. Ghanem R, Spanos P. *Stochastic Finite Elements*: *A Spectral Approach* (1991 edn). Springer: Berlin, 1991.
8. Ma X, Zabaras N. A stabalized stochastic finite element second-order projection method for modeling natural convection in random porous media. *Journal of Computational Physics* 2008; **227**:8448–8471.
9. Asokan B, Zabaras N. Using stochastic analysis to capture unstable equilibrium in natural convection. *Journal of Computational Physics* 2005; **208**:134–153.
10. Acharjee S, Zabaras N. Uncertainty propagation in finite deformations—a spectral Lagrangian approach. *Computer Methods in Applied Mechanics and Engineering* 2006; **195**:2289–2312.
11. Xiu D, Karniadakis G. Modeling uncertainty in flow simulations via generalized polynomial chaos. *Journal of Computational Physics* 2003; **187**:137–167.
12. Field R, Grigoriu M. On the accuracy of the polynomial chaos approximation. *Probabilistic Engineering Mechanics* 2004; **19**:65–80.
13. Ma X, Zabaras N. An adaptive high-dimensional stochastic model representation technique for the solution of stochastic partial differential equations. *Journal of Computational Physics* 2010; **229**:3884–3915.
14. Belytschko T, Liu W, Moran B. *Nonlinear Finite Elements for Continua and Structures*, Chapter 6.7. Wiley: New York, 2000.
15. Jirasek M, Bazant Z. *Inelastic Analysis of Structures*, Chapter 26. Wiley: New York, 2002.
16. Zukas J. *Introduction to Hydrocodes*, Chapter 4. Elsevier: New York, 2004.
17. Bishop J. Simulating the pervasive fracture of materials and structures using randomly close packed Voronoi tessellations. *Computational Mechanics* 2009; **44**:455–471.
18. Grady D. *Fragementation of Rings and Shells*: *The Legacy of N.F. Mott*. Springer: Berlin, 2006.
19. Roy C, Oberkampf W. A complete framework for verification, validation, and uncertainty quantification in scientific computing. *The 48th AIAA Aerospace Sciences Meeting Including the New Horizons Forum and Aerospace Exposition*, Orlando, FL, 2010, AIAA 2010-124.

DOI: 10.1002/nme

20. Oberkampf W, Roy C. *Verification and Validation in Scientific Computing*, Chapter 12.8. Cambridge University Press: New York, 2010.
21. Lindgren B. *Statistical Theory* (4th edn). Chapman & Hall/CRC: New York, 1993.
22. Rosenthal J. *A First Look at Rigorous Probability Theory*. World Scientific Publishing: Hackensack, New Jersey, 2006.
23. Haldar A, Mahadevan S. *Probability*, *Reliability*, *and Statistical Methods in Engineering Design*, Chapter 4.5.6. Wiley: New York, 2000.
24. Resnick S. *A Probability Path*. Birkhäuser: Boston, 1998.
25. Kolmogorov A. Sulla determinazione empirica di una legge di distribuzione. *Giornale dell'Istituto Italiano degli Attuari* 1933; **4**:83–91.
26. Gibbons J, Chakraborti S. *Nonparametric Statistical Inference*. Marcel Dekker, Inc.: New York, 2005.
27. Kendall M, Stuart A. *The Advanced Theory of Statistics* (3rd edn), vol. 2. Hafner Publishing Company: New York, 1973; 466–474.
28. Birnbaum Z. Numerical tabulation of the distribution of Kolmogorov's statistic for finite sample size. *Journal of the American Statistical Association* 1952; **47**:425–441.
29. Lohr S. *Sampling*: *Design and Analysis* (2nd edn). Brooks/Cole Cengage Learning: Boston, MA, 2010.
30. Srinivasan R. *Importance Sampling—Applications in Communications and Detection*. Springer: Berlin, 2002.
31. Alf C, Lohr S. Sampling assumptions in introductory statistics classes. *The American Statistician* 2007; **61**(1): 71–77.
32. Fulks W. *Advanced Calculus*: *An Introduction to Analysis* (3rd edn). Wiley: New York, 1978.
33. Matlab. The Mathworks, Inc. Available from: http://www.mathworks.com.
34. Strogatz S. *Nonlinear Dynamics and Chaos with Applications to Physics*, *Biology*, *Chemistry*, *and Engineering*, Chapter 9. Westview Press: Cambridge, MA, 1994.
35. Lasota A, Mackey M. *Chaos*, *Fractals*, *and Noise*: *Stochastic Aspects of Dynamics* (2nd edn). Springer: New York, 1994.
36. Peitgen H, Jürgens H, Saupe D. *Chaos and Fractals*: *New Frontiers of Science*, Chapter 10. Springer: New York, 1992.
37. Schuster H, Just W. *Deterministic Chaos*, *An Introduction* (4th edn), Chapter 9. Wiley-VCH Verlag GmbH & Co. KGaA: Weinheim, 2005.
38. Grady D, Benson D. Fragmentation of metal rings by electromagnetic loading. *Experimental Mechanics* 1983; **23**:393–400.
39. Robinson A *et al.* ALEGRA: an arbitrary Lagrangian–Eulerian multimaterial multiphysics code. *Proceedings of the 46th AIAA Aerospace Science Meeting*, January 2008, AIAA-2008-1235.
40. Needleman A. Material rate dependence and mesh sensitivity in localization problems. *Computer Methods in Applied Mechanics and Engineering* 1988; **67**(1):69–85.
41. Bazant Z, Jirasek M. Nonlocal integral formulations of plasticity and damage: survey of progress. *Journal of Engineering Mechanics* 2002; **128**(11):1119–1149.
42. Grady D, Kipp M. Mechanisms of dynamic fragmentation: factors governing fragment size. *Mechanics of Materials* 1985; **4**:311–320.
43. Brannon R, Wells J, Strack O. Validating theories for brittle damage. *Metallurgical and Materials Transactions A* 2007; **38**:2861–2868.
44. Zhang H, Ravi-Chandar K. On the dynamics of necking and fragmentation II. Effect of material properties, geometrical constraints and absolute size. *International Journal of Fracture* 2008; **150**:3–36.
45. Johnson G, Cook W. A constitutive model and data for metals subjected to large strains, high strain rates, and high temperatures. *The Seventh International Symposium on Ballistics*, The Hague, The Netherlands, 1983.
46. Sagan H. *Space-filling Curves*, Chapter 2. Springer: Berlin, 1994.
47. Paraview. Available from: http://www.paraview.org.
48. Luenberger D. *Linear and Nonlinear Programming* (2nd edn), Chapter 10. Kluwer Academic Publishers: Boston, 2003.

DOI: 10.1002/nme